

Politecnico di Torino





Politecnico di Torino

Dipartimento di Ingegneria Meccanica e Aerospaziale

Corso di laurea magistrale in Ingegneria Biomedica

Superparamagnetic Iron Oxide Nanoparticles as a Promising Platform for Dual T_1/T_2 MRI and Future Theranostic Applications

Relatori:

Prof.ssa Valentina Alice Cauda

Candidata:

Luna Lanzi 325228

Correlatori:

Dott. Fernando Herranz Rabanal

Anno Accademico 2025/2026

"Niente nella vita va temuto,

dev'essere solamente compreso.

Ora è tempo di comprendere di più,

così possiamo temere di meno. "

Marie Curie

Index

i. List of Abbreviations....3
ii. List of Figures....5
iii. List of Tables....10
Abstract....12
1 Introduction....13
1.1 Nanomedicine and Theranostic Nanoparticles....13
1.2 Applications of nanomaterials in the biomedical field....15
1.3 Iron Oxide Nanoparticles: physico-chemical properties and applications in Nanomedicine....17
1.3.1 Principles of Magnetic Resonance Imaging and the role of IONPs as contrast agents....19
1.4 Surface engineering: functionalization and bioconjugation strategies....22
1.4.1 The role of the protein corona and stability in biological environments....22
1.4.2 Albumin as a smart vector....23
1.4.3 Bioconjugation chemistry: covalent functionalization via carbodiimide chemistry....25
1.5 Preliminary studies....27
1.6 Objectives....30
2 Materials And Methods....32
2.1 Synthesis and Purification of Iron Oxide Nanoparticles....32
2.2 Elemental Analysis by Inductively Coupled Plasma Optical Emission Spectrometry....34
2.3 Dimensional Analysis and Colloidal Stability....35
2.4 Fourier Transform Infrared Spectroscopy....37
2.5 NMR relaxometry studies....39
2.6 Evaluation of Contrast Efficacy (MRI Phantom)....41
2.7 Functionalization of Nanoparticles with BSA....43
2.7.1 Sample Selection and Synthesis....44
2.7.2 Buffer Exchange and Carboxylic Group Activation (EDC/NHS)....45

2.7.3 Bioconjugation in HEPES and Final Purification in Water 46
2.7.4 Protein Quantification via Bradford Assay and UV-Visible Spectrophotometry 47
3 Results And Discussion 51
3.1 Colloidal Stability: Evolution of Hydrodynamic Size and Zeta Potential over time 51
3.2 Quantification by Inductively Coupled Plasma Optical Emission Spectrometry 55
3.3 Functional and surface characterization by FTIR spectroscopy 58
3.4 Evaluation of relaxometric properties 61
3.5 Tomographic Evaluation on Phantoms (7 T MRI) 65
3.6 Outcomes of functionalization via BSA 67
4 Conclusions 71
5 Future Perspectives 73
5.1 Dimensional and synthetic optimization 73
5.2 Advanced structural and morphological characterization 73
5.3 Stability studies and active functionalization 74
5.4 Preclinical validation for glioblastoma: *in vitro* and *in vivo* 75
Bibliography 76

i. List of Abbreviations

BBB – Blood-Brain Barrier

Hc – Coercivity

BSA – Bovine Serum Albumin

DLS – Dynamic Light Scattering

DMEM – Dulbecco's Modified Eagle Medium

EDC – 1-ethyl-3-(3-dimethylaminopropyl) carbodiimide

EPR – Enhanced Permeability and Retention

FBS – Fetal Bovine Serum

FTIR ATR – Attenuated Total Reflectance - Fourier Transform Infrared Spectroscopy

GBM – Glioblastoma Multiforme

HAADF-STEM – High-Angle Annular Dark-Field Scanning Transmission Electron Microscopy

HAS – Human Serum Albumin

HEPES – 4-(2-hydroxyethyl)-1-piperazineethanesulfonic acid

ICP-OES – Inductively Coupled Plasma Optical Emission Spectrometry

IONP – Iron Oxide Nanoparticle

Ms – Saturation Magnetization

Mr – Remanent Magnetization

MRI – Magnetic Resonance Imaging

Mz - Magnetization Vector

NHS – N-hydroxysuccinimide

NMR – Nuclear Magnetic Resonance

PAMPA – Parallel Artificial Membrane Permeability Assay

PDI – Polydispersity Index

PET – Positron Emission Tomography

R_1 – Longitudinal relaxation rate

R_2 – Transverse relaxation rate

r_1 – Longitudinal relaxivity

r_2 – Transverse relaxivity

RES – Reticuloendothelial System

RF – Radiofrequency

SEC – Size Exclusion Chromatography

SPECT – Single Photon Emission Computed Tomography

SPARC – Secreted Protein Acidic and Rich in Cysteine

SPION – Superparamagnetic Iron Oxide Nanoparticle

STEM – Scanning Transmission Electron Microscopy

T_1 – Spin-lattice relaxation time / Longitudinal relaxation time

T_2 – Spin-spin relaxation time / Transverse relaxation time

TEM – Transmission Electron Microscopy

TGA – Thermogravimetric Analysis

VSM – Vibrating Sample Magnetometry

XRD – X-ray Diffraction

ii. List of Figures

Figure 1.1: Annual trend and global growth of the body of scientific publications related to the use of nanomaterials and drug delivery systems in the oncological field between 2003 and 2024. This increase highlights the progressive consolidation of nanotechnologies within the international scientific literature [1]. 13

Figure 1.2: Magnetic behavior under the influence of an external field. The x-axis represents the applied field while the y-axis indicates the magnetization of the sample. The red curve exhibits a hysteresis loop, typical of ferromagnetic materials, where the associated figures of merit are the Ms, Mr, and Hc. In contrast, the green curve displays the response of superparamagnetic nanoparticles to an external field, which follows a sigmoidal trend without hysteresis. The diagram also shows the linear responses characteristic of paramagnetic (blue line) and diamagnetic (black line) materials [2]. ..19

Figure 1.3: Physical principles of Nuclear Magnetic Resonance (NMR). (**A**) Without any applied stimuli, the magnetic moments of protons are randomly oriented; exciting the system with a static magnetic field, a parallel or antiparallel alignment is inducted, generating a longitudinal magnetization vector (Mz). (**B**) The application of a RF pulse deflects the Mz vector and generates a magnetization component in the transverse plane (Mxy). When the pulse ends, the system returns to equilibrium. (**C**) Temporal dynamics of the relaxation processes: the longitudinal recovery curve (T_1, time required to restore 63% of Mz) and the free induction decay curves (T_2, time in which Mxy decays to 37% of its maximum value). Images were created using BioRender.com. 21

Figure 1.4: Crystallographic structure of BSA. The macromolecule presents a globular conformation consisting of approximately 67% α-helix secondary structures, organized into three main domains. This spatial architecture guarantees the exposure on the external surface of numerous lysine residues (free primary amino groups), which act as essential reactive sites for covalent anchoring to the nanoparticles [3]. 24

Figure 1.5: Representation of the molecular mechanism of zero-length bioconjugation mediated by EDC/NHS. This process illustrates the preliminary activation of the surface carboxylic group by EDC with the formation of the O-acylisourea intermediate, the subsequent stabilizing transesterification operated by NHS with the release of the urea derivative, and the conclusive nucleophilic attack guided by the primary amines (lysines) of BSA for the generation of the definitive covalent amide bond [38]. 27
Figure 1.6: Magnetization curves acquired by VSM. The graph illustrates the specific magnetization (expressed in $Am^2/kgFe$) as a function of the applied magnetic field (H, in kA/m) for the control nanoparticles (MW-IONP) and for the formulations synthesized in silicone oil at different reaction times (10, 45, and 120 minutes). The absence of a measurable hysteresis loop (zero coercivity and remanence) confirms the superparamagnetic behavior of the investigated nanosystems at room temperature [4], [5]. 29
Figure 2.1: Schematic of the synthetic and purification protocol for IONPs. The process is divided into four main phases: (**1**) addition of inorganic precursors and doping agents (Mg^{2+} or Co^{2+}); (**2**) synthesis in a silicone bath at 100 °C with hydrazine injection; (**3**) kinetic blocking of the reaction by means of an ice-water bath; and (**4**) purification by size exclusion chromatography (SEC) using PD-10 columns with elution in Milli-Q water. Figure produced with Biorender.com. 32
Figure 2.2: Schematic representation of the main molecular vibrational modes involved in the absorption of infrared radiation. Stretching vibrations involve a change in the bond length along its axis, whereas bending vibrations involve a change in the bond angle. These motions are responsible for generating the absorption peaks in the FTIR-ATR spectrum [44]. 38
Figure 2.3: Lyophilization steps for FTIR sample preparation. (**A**) Glass vials containing the samples right after freezing in liquid nitrogen. The openings are covered with a breathable material to allow for proper solvent (Milli-Q water) sublimation. (**B**) Primary drying phase. The samples are placed inside glass flasks attached to a benchtop freeze-

dryer (BenchTop Pro, SP Scientific). The display shows the operating parameters (pressure and condenser temperature). (**C**) Macroscopic appearance of the final freeze-dried product, showing a solid and porous consistency, ready for analysis. 39
Figure 2.4: Schematic representation of the surface functionalization process showing the final biocompatible nano-complex (BSA IONP 20 mM Mg^{2+}). Figure produced with Biorender.com.....44
Figure 2.5: Explanatory diagram of the activation process. Figure produced with Biorender.com.....45
Figure 2.6: Explanatory diagram of the filtration process through centrifugation and resuspension in HEPES buffer. Figure produced with Biorender.com.....46
Figure 2.7: Explanatory diagram of the filtration process through centrifugation and resuspension in MILLI-Q water. Figure produced with Biorender.com. 47
Figure 3.1: Colloidal characterization over time (up to 15 days) of undoped iron oxide nanoparticles (control) and doped with Cobalt ions (Co^{2+}) and magnesium ions (Mg^{2+}) at different concentrations (6, 12, and 20 mM), synthesized at 100 °C for a reaction time of 45 and 60 minutes. (**A**) Trend of the hydrodynamic diameter (Size, nm) measured by DLS for nanoparticles containing ions Co^{2+} at 45 minutes. (**B**) Evolution of the Zeta potential (ζ, mV) measured by laser Doppler micro-electrophoresis for the evaluation of surface stability and electrostatic charge in NaCl suspension for nanoparticles containing Co^{2+} at 45 minutes. (**C**) Trend of the hydrodynamic diameter (Size, nm) measured by DLS for nanoparticles containing ions Mg^{2+} at 45 minutes. (**D**) Evolution of the Zeta potential (ζ, mV) measured by laser Doppler micro-electrophoresis for the evaluation of surface stability and electrostatic charge in NaCl suspension for nanoparticles containing Mg^{2+} at 45 minutes. (**E**) Trend of the hydrodynamic diameter (Size, nm) measured by DLS for nanoparticles containing ions Mg^{2+} at 60 minutes. (**F**) Evolution of the Zeta potential (ζ, mV) measured by laser Doppler micro-electrophoresis for the evaluation of surface stability and electrostatic charge in NaCl suspension for nanoparticles containing Mg^{2+} at 60 minutes. Plots produced using GraphPad Prism 8.....53

Figure 3.2: Evaluation of PDI for the different nanoparticle formulations. (**A**) PDI values relating to the syntheses conducted for 45 minutes: comparison between the undoped control and the samples doped with magnesium (Mg^{2+}) or cobalt (Co^{2+}) ions at increasing concentrations (6, 12, and 20 mM). (**B**) PDI values relating to the optimized syntheses at 60 minutes: comparison between the control and the samples doped with magnesium ions at 12 and 20 mM. Plots produced using GraphPad Prism 8. 54

Figure 3.3: FTIR transmittance spectra of nanoparticles. The graphs compare the control formulations with the samples synthesized in the presence of heterometallic cations at increasing concentrations (6, 12, and 20 mM). The top panels (**B, C**) show the effect of magnesium doping for the syntheses conducted at 100 °C for 45 and 60 minutes. The **A** panel illustrates the impact of cobalt doping (synthesis at 45 minutes). Plots produced using GraphPad Prism 8. 60

Figure 3.4: The graphs illustrate the linear regressions of the longitudinal ($1/T1 - 1/T1w$) and transverse ($1/T2 - 1/T2w$) relaxation rates as a function of the total metal concentration ($Fe + M$, expressed in mM), from whose slopes the respective values of specific relaxivity and were extrapolated. Specifically, panels (**A**) and (**B**) show the trend of the relaxation rates for the 45-minute synthesis set, comparing the control IONPs with those doped with magnesium at increasing concentrations (from 6 to 20 mM). Panels (**C**) and (**D**) report the effect of cobalt doping, maintaining the same synthesis time at 45 minutes. Panels (**E**) and (**F**) illustrate instead the results for the formulations synthesized at 100 °C for 60 minutes with magnesium. Finally, panel (**G**) presents a summary histogram of the ratio $r2/r1$ all the analyzed samples. Plots produced using GraphPad Prism 8. 64

Figure 3.5: Tomographic acquisition weighted in $T1$ (FLASH sequence at 7 T) for the evaluation of the relaxivity effect $r1$ at different Fe concentrations arranged from left to right: Milli-Q water, 1.5, 3, and 8 mM Fe. 66

Figure 3.6: T_2-weighted tomographic acquisition (FLASH sequence at 7 T) for the evaluation of the relaxivity effect r_2 at different Fe concentrations arranged from left to right: Milli-Q water, 1.5, 3, and 8 mM Fe. 67

Figure 3.7: Standard calibration curve for protein quantification via the Bradford colorimetric assay. The graph illustrates the linear correlation between the absorbance, measured with a spectrophotometer at a wavelength of 595 nm, and the known concentration of the standard protein (in mg/mL). The interpolation of the experimental data generated the equation line $y = 0.2536x + 0.0081$, characterized by a coefficient $R2$ equal to 0.9984 68

Figure 3.8: FTIR transmittance spectrum of iron oxide nanoparticles Mg^{2+} (60 min) functionalized with BSA and respective controls. Plots produced using GraphPad Prism 8 70

iii. List of Tables

Table 3-1: The table summarizes the quantitative data extrapolated from the ICP-OES analysis (real concentration in mg/L and mM, heteroatom/iron molar ratio, and percentage incorporation efficiency) of iron (Fe), magnesium (Mg^{2+}), and cobalt (Co^{2+}) determined by ICP-OES spectrometry for the different IONP formulations. The samples are divided based on the hydrothermal synthesis time (45 and 60 minutes at 100 °C). The highlighted row indicates the samples selected for subsequent relaxometry and infrared spectroscopy studies. 56

Table 3-2: Relaxometric parameters of the superparamagnetic nanoparticle formulations synthesized at 100 °C. The table reports the values of specific longitudinal and transverse relaxivity, expressed in $mM^{-1}s^{-1}$, together with the dimensionless ratio $r2/r1$ calculated for each formulation. The data are divided based on the thermal reaction time (45 and 60 minutes) and compare the undoped control samples with the formulations doped with magnesium and cobalt ions at increasing concentrations (6, 12, and 20 mM). The specific values were analytically extrapolated from the slopes of the linear regression lines of the respective relaxation rates as a function of the total metal concentration. 62

Table 3-3: Absolute values of the relaxation times and rates instrumentally recorded for the optimized IONP Mg^{2+} 20 mM formulation synthesized at 60 minutes. The table summarizes the T1 and T2 relaxation times, expressed in milliseconds, with the corresponding absolute relaxation rates (R1 and R2, expressed in s^{-1}) measured at different sample dilutions. 65

Table 3-4: Summary of the nanoparticle functionalization data with BSA over time (0, 6, and 24 hours). For the three analyzed formulations (control, physisorption with BSA alone, and covalent activation with BSA+EDC/NHS), the measured protein concentration ([]BSA, mg/mL), the Encapsulation Efficiency, and the absolute mass of bound protein (mg) are reported. The abbreviation N.D. (Not Detectable) indicates an absorbance below the detection limit of the instrument, confirming the absence of bound

protein; consequently, the wording N.A. (Not Applicable) indicates the mathematical impossibility of calculating the %EE starting from a zero protein mass. 69

Abstract

Superparamagnetic iron oxide nanoparticles (SPIONs) find applicability in the field of theranostics due to their biological tolerability and their magnetic properties. This work focuses on the development of SPIONs doped with increasing concentrations of Mg^{2+} and Co^{2+} ions, with the aim of modulating and optimizing contrast efficiency in magnetic resonance imaging (MRI). The experimental activity is divided into two main phases: SPION synthesis and surface functionalisation. The first phase consisted of synthesizing the inorganic nanoparticles using varying metal doping dosage. Subsequently the samples were subjected to a physicochemical characterization to define their size distribution and colloidal stability. To evaluate the magnetic performance of the samples, NMR relaxometry techniques were used, which allowed the extrapolation of the T_1 and T_2 relaxation times. Consequently, from the calculation of the transverse relaxivity (r_2), it was possible to evaluate the direct impact of the metals inserted into the crystal lattice. The subsequent MRI analyses on phantoms were used to test the imaging performance of the samples, demonstrating the capacity of the nanoparticles to provide simultaneous T_1 and T_2 contrast. In the final phase of the work, in order to improve the biological interface of the system, the nanoparticles were modified by introducing a bovine serum albumin (BSA) coating. The obtained results provide a methodological pathway showing how the control of the inorganic core architecture, followed by surface functionalization, is an essential step for the design of stable systems, ideal for precision imaging and drug delivery. Finally, surface engineering with BSA grants the system greater stability and stealth properties, fundamental characteristics for future theranostic applications aimed at crossing the blood brain barrier and targeting aggressive tumors such as glioblastoma multiforme.

1 Introduction

1.1 Nanomedicine and Theranostic Nanoparticles

The application of nanotechnology principles in biomedical sciences has opened new horizons in the field of drug delivery and diagnostics, consolidating it into the discipline of nanomedicine aimed at improving individual health (**Figure 1.1**) [1].

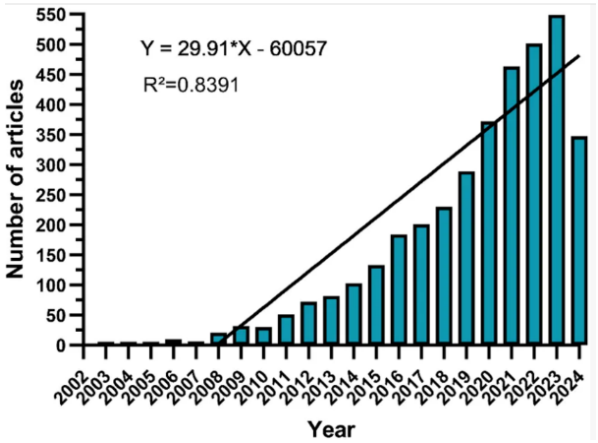


Figure 1.1: Annual trend and global growth of the body of scientific publications related to the use of nanomaterials and drug delivery systems in the oncological field between 2003 and 2024. This increase highlights the progressive consolidation of nanotechnologies within the international scientific literature [1].

The development of this field stems from the need to overcome the biopharmaceutical, pharmacokinetic, and pharmacodynamic limitations that characterize conventional therapeutic agents. In most cases, the high lipophilicity of these drugs compromises their aqueous solubility in biological fluids, limiting their permeability. Their potential is further hindered by chemical instability, low bioavailability, and rapid blood clearance, linked to the rapid processes of enzymatic degradation and renal excretion [6]. The primary clinical limitation lies in the non-specific volume of distribution: the absence of molecular directionality causes the drug to diffuse indiscriminately in all body compartments. This entails that only a fraction of the administered dose reaches the site

of action, while the remaining part exposes healthy tissues to cytotoxic agents, causing severe adverse effects typical of chemotherapeutic regimens [6].

To overcome these issues, the nanomedical approach resorts to engineering nanovectors. These delivery systems, characterized by dimensions ranging between 1 and 100 nm, exhibit high surface-to-volume ratios. This peculiarity allows encapsulation of the active principle within them or anchoring a high quantity of it on their surface, making them extremely versatile tools for multiple biomedical applications [7] . The use of this strategy allows isolating the drug from the blood microenvironment, preventing its premature degradation, and simultaneously guaranteeing accurate control over both spatial and temporal release kinetics.

In the oncological field, the rationale for the use of nanovectors is based on an anatomical and physiological anomaly typical of the tumor stroma, defined as the Enhanced Permeability and Retention (EPR) Effect [8]. The revolutionary work of Maeda and Matsumura demonstrated that the rapid and uncontrolled proliferation of neoplastic cells generates a state of local hypoxia, which triggers disordered neoangiogenesis [8]. Unlike healthy capillaries, the endothelium of tumor blood vessels is chaotic and structurally incomplete with wide intercellular fenestrations. Concomitant with this vascular hyperpermeability, the tumor tissue is characterized by a dysfunctional lymphatic system, which is unable to effectively drain macromolecules from the interstitial space, thus causing their increased accumulation [8], [9]. This allows nanoparticles to selectively extravasate from the bloodstream towards the neoplastic interstitium, progressively accumulating there over time. The literature agrees that the dimensional confinement of the nanocarrier is the primary parameter for optimizing the EPR effect [8]: excessively small systems undergo rapid renal clearance, while excessively voluminous architectures are intercepted by the immune system or fail to penetrate the dense extracellular matrix of the tumor [9].

Despite the advantages offered by passive delivery, clinical translation has highlighted the need to monitor in real-time the *in vivo* fate of the nanocarrier to evaluate their actual intratumoral accumulation. From this need arises the concept of "Theranostics" an approach that merges diagnostic and therapeutic capabilities within a single entity [10]. By its nature, a theranostic platform based on nanoparticles is a multi-component system[10]. Its typical architecture involves a core endowed with intrinsic physicochemical properties that allow the generation of a signal detectable by biomedical imaging techniques that can act as a reservoir for therapeutic agents. This core is surrounded by an engineered shell designed to ensure the biocompatibility of the complex and host additional pharmacological payloads [11], [12]. This hybrid construct aims at a threefold objective [10], [12]:

- Spatially localize the pathology, identifying its exact location.
- Track the biodistribution, monitoring how the treatment behaves within the organism.
- Induce a targeted drug release, laying the foundations for personalized therapeutic regimens.

The data obtained from these platforms offer concrete support to guide clinical choices in a more precise and specific manner for individual patients, ultimately contributing to a clear improvement in therapeutic outcomes.

1.2 Applications of nanomaterials in the biomedical field

The wide range of nanomaterials available has enabled a diverse array of translational applications. The ability to modify their composition, morphology, surface potential, and specific surface area makes these systems adaptable probes suitable for a broad variety of biomedical applications [13].

In the context of drug delivery, research has evolved beyond the limitations of passive accumulation to favor active targeting strategies [8], [13]. This approach aims to maximize the affinity and selectivity between the vector and pathological cells through appropriate surface functionalization of the nanoparticle. The anchoring of specific ligands allows for recognition and direct interaction with receptors on the target membrane. Subsequent receptor activation promotes the internalization of the nanocarrier into the intracellular compartment, triggering specific signal transduction cascades capable of modulating fundamental biological responses, such as cell proliferation, migration, and death. By utilizing molecules such as monoclonal antibodies, peptides, or aptamers, the nanocarrier is functionalized to selectively recognize membrane receptors that are significantly overexpressed on the target cell surface compared to healthy epithelium [13], [14]. Antigen–antibody or ligand-receptor binding initiates cellular internalization mechanisms, typically via receptor-mediated endocytosis. This process transfers the nanovehicle directly into the compartment of interest, ensuring that the release occurs precisely at the site of action [14].

Beyond their transport function, specific classes of nanomaterials possess intrinsic physical properties that enable them to exert a direct therapeutic action. Local ablative therapies, such as magnetic or plasmonic hyperthermia, represent a primary branch of research [15]. Metallic nanoparticles or magnetic oxides can interact with non-invasive external electromagnetic fields (such as near-infrared laser radiation or alternating radiofrequency magnetic fields), absorbing their energy and dissipating it as heat [15]. At the intratumoral level, the application of this stimulus generates a localized temperature increase that alters cell membrane fluidity and denatures proteins. This induces apoptosis in neoplastic cells while preventing thermal damage to the surrounding healthy tissues [15].

In the diagnostic field, the introduction of nanomaterials has revolutionized molecular imaging. Unlike traditional molecular contrast agents, which undergo rapid tissue dispersion, nanoparticles ensure a high signal-to-noise ratio owing to the high concentration of the active center [16]. By modulating the core composition, it is possible to generate highly specific tracers for nuclear tomographic methods (Positron Emission Tomography (PET) and Single Photon Emission Computed Tomography (SPECT)), optical imaging, and resonance techniques [4], [17]. To date, advanced synthesis is moving toward multimodal probes, namely complex architectures capable of integrating radionuclides and paramagnetic materials that simultaneously offer the quantitative detection sensitivity of PET and the superior morphological resolution provided by Magnetic Resonance Imaging (MRI) [4], [17], [18].

1.3 Iron Oxide Nanoparticles: physico-chemical properties and applications in Nanomedicine

Among the various nanomaterials studied for biomedical applications, IONPs, based on crystalline cores of magnetite (Fe_3O_4) and maghemite (γ-Fe_2O_3), play a leading role [19]. The primary distinction between the two phases lies in their composition: magnetite contains a mixture of Fe^{2+} and Fe^{3+} ions, while maghemite consists exclusively of Fe^{3+} ions accompanied by structural vacancies in the crystal lattice [19]. The interest in these structures is justified by their physico-chemical characteristics, notably their intrinsic magnetic properties and an excellent biocompatibility profile, factors that allow their use in a wide range of biomedical applications [20], [21].

The biocompatibility of IONPs stems from the endogenous nature of iron, an element essential for human cellular metabolism [22]. At the end of their circulatory function, these nanoparticles are recognized and internalized via phagocytosis by macrophages of the reticuloendothelial system (located primarily in the liver and spleen). Within the

hydrolytic and acidic environment of macrophage lysosomes, the crystal lattice is progressively degraded, releasing free Fe^{2+} and Fe^{3+} ions [21], [22]. The excess released iron does not trigger systemic cytotoxicity; rather, it is intercepted by natural iron homeostasis mechanisms. This degradative pathway has historically allowed specific IONP formulations to pass rigorous toxicity tests required for clinical approval by international regulatory agencies [20].

From the perspective of solid-state physics, the magnetic behavior of IONPs is correlated with the dimensions of the inorganic lattice. When the particle diameter is confined below a certain critical size, the material ceases to form multiple magnetic domains and becomes a single domain [23]. In this context, thermal fluctuations induce a rapid and spontaneous reversal of the magnetic moments. This phenomenon leads to the transition from a ferromagnetic to a superparamagnetic state, characteristic of Superparamagnetic Iron Oxide Nanoparticles (SPIONs) [23]. Macroscopically, a superparamagnetic material exhibits high saturation magnetization in the presence of an external magnetic field, but the hysteresis loop passes exactly through the origin, indicating a total absence of residual magnetization (remanence) upon removal of the field (**Figure 1.2**) [19], [23]. This instantaneous magnetic reversibility is an unquestionable prerequisite for intravenous application, as it prevents dipolar interactions between particles in the bloodstream, eliminating the potential for aggregation that could cause vascular occlusions [19].

In addition to ensuring intravascular safety, this intrinsic superparamagnetism allows for direct manipulation via external magnetic fields. This magnetic response serves a dual purpose: on one hand, it enables the generation of signals in MRI, optimizing diagnostic capabilities; on the other hand, it makes magnetic drug targeting possible [19], [24]. Furthermore, heat generation via hyperthermia and the local release of iron inherently act as additional therapeutic mechanisms against pathology. Finally, the exceptional versatility of these structures is consolidated by their responsiveness to

external fields through relaxation mechanisms, combined with their ability to maintain perfect stability in solution without undergoing precipitation [21].

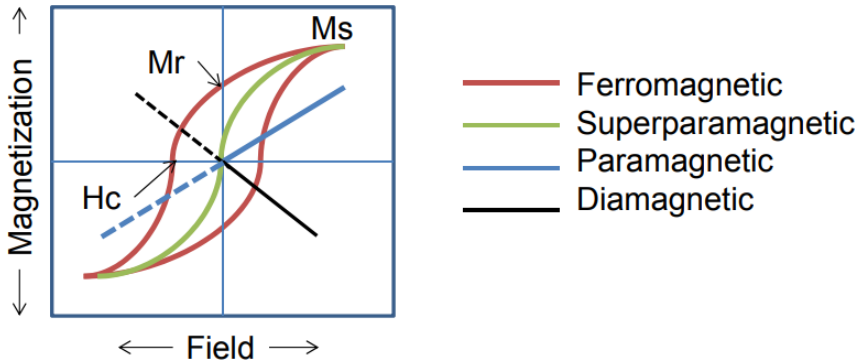


Figure 1.2: Magnetic behavior under the influence of an external field. The x-axis represents the applied field while the y-axis indicates the magnetization of the sample. The red curve exhibits a hysteresis loop, typical of ferromagnetic materials, where the associated figures of merit are the Ms, Mr, and Hc. In contrast, the green curve displays the response of superparamagnetic nanoparticles to an external field, which follows a sigmoidal trend without hysteresis. The diagram also shows the linear responses characteristic of paramagnetic (blue line) and diamagnetic (black line) materials [2].

1.3.1 Principles of Magnetic Resonance Imaging and the role of IONPs as contrast agents

The main application of IONPs is related to MRI. MRI is a tomographic technique based on the principles of nuclear magnetic resonance (NMR), which provides high spatial resolution and tissue contrast images without the use of ionizing radiation [25]. This technique relies on the interaction between the magnetic moments of water protons present in tissues and a static magnetic field (B_0). The protons aligned with the field are perturbed by the application of a radiofrequency (RF) pulse. At the end of the pulse, the protons absorb energy and move out of the equilibrium condition, returning to it through relaxation mechanisms (**Figure 1.3**) [25]:

- Longitudinal relaxation (T_1): also known as spin-lattice relaxation, it measures the time required for protons to release energy to the surrounding environment, restoring the component of magnetization parallel to the field B_0. This is a relatively slow process because the excited protons must gradually transfer their excess energy to the adjacent molecular structure. Consequently, the duration of this relaxation is closely linked to the efficiency of the interactions between ^1H nuclei and the local microenvironment; a less effective energy exchange physiologically determines more prolonged T_1 relaxation times [25].
- Transverse relaxation (T_2): known as spin-spin relaxation, it quantifies the loss of phase coherence among adjacent magnetic moments in the transverse plane caused by mutual magnetic interactions and local field inhomogeneity. Unlike the former, this is a decidedly faster phenomenon because it is governed by direct interactions between neighboring ^1H nuclei, rather than by the transfer of energy to the surrounding molecular lattice. For this reason, T_2 relaxation times are typically much shorter than those recorded for T_1 [25].

Contrast agents are used to accentuate the diagnostic differences between healthy and altered tissues[26], [27]. The latter acts as a catalyst for proton relaxation. The efficiency of an agent is described by its relaxivity (longitudinal relaxivity (r_1) or transverse relaxivity (r_2) measured in $mM^{-1}s^{-1}$), which defines the increase in the relaxation rate per unit of concentration of the active metal [26], [27]. Contrast agents are divided into two classes [26], [27], [28]:

- Positive contrast agents: traditionally, these are paramagnetic complexes based on gadolinium (Gd^{3+}) that act by shortening T_1 through inter-sphere interactions. The acceleration of the longitudinal recovery generates an increase in the signal intensity, visualized as a brighter area. However, serious issues remain related to the potential toxicological accumulation of these agents *in vivo*, which has

stimulated the development of alternative nanotechnological formulations [25], [28].

- Negative contrast agents: these are characterized by high magnetic susceptibility that generates strong microscopic magnetic field gradients (distal field effects) and accelerates the dephasing of water spins, causing the collapse of the T_2 parameter. This results in a clear signal drop, visible as a dark area (hypointensity) in the diagnostic image [27], [28].

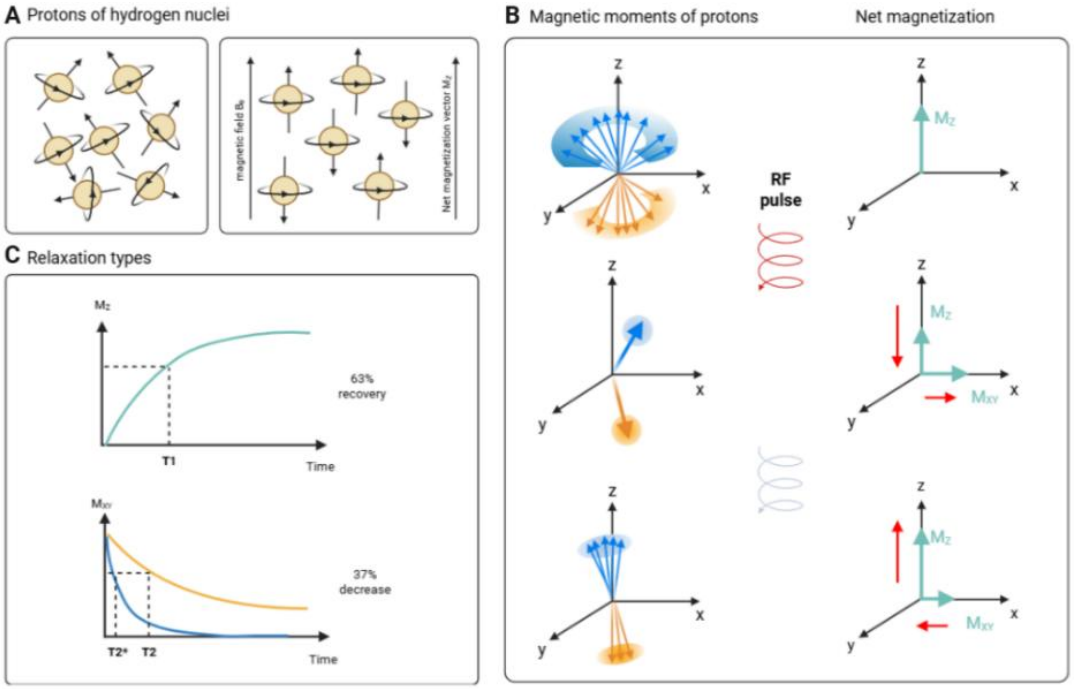


Figure 1.3: Physical principles of Nuclear Magnetic Resonance (NMR). (**A**) Without any applied stimuli, the magnetic moments of protons are randomly oriented; exciting the system with a static magnetic field, a parallel or antiparallel alignment is inducted, generating a longitudinal magnetization vector (Mz). (**B**) The application of a RF pulse deflects the Mz vector and generates a magnetization component in the transverse plane (Mxy). When the pulse ends, the system returns to equilibrium. (**C**) Temporal dynamics of the relaxation processes: the longitudinal recovery curve (T_1, time required to restore 63% of Mz) and the free induction decay curves (T_2, time in which Mxy decays to 37% of its maximum value). Images were created using BioRender.com.

SPIONs are the gold standard for negative contrast. For a nanocarrier to excel in this regime, a high absolute value of r_2 is not sufficient, but it is essential to obtain a high r_2/r_1 ratio [26]. A high ratio ensures that the main effect of the phase coherence loss is not counterbalanced by the simultaneous recovery of the longitudinal signal. The controlled alteration of the inorganic core dimensions, modification of the thickness and water permeability of the coating, and introduction of heterometallic doping within the iron oxide lattice constitute the modulable engineering parameters to maximize contrast performance [5], [28].

1.4 Surface engineering: functionalization and bioconjugation strategies

To increase the effectiveness of a platform of this type, and with it the biocompatibility and *in vivo* biodistribution, surface engineering becomes a necessary step; the thermodynamic interactions at the interface between the nanoparticle surface and the host biological environment determine its entire pharmacokinetic profile and guarantee the required stealth properties [29].

1.4.1 The role of the protein corona and stability in biological environments

Following synthesis, nanoparticles exhibit a high surface free energy. When inserted into media with high ionic strength, Van der Waals forces and hydrophobic interactions arise, leading to rapid colloidal coagulation [30]. In addition, introduction into the blood plasma exposes the particles to a heterogeneous protein environment. Due to the Vroman effect, serum proteins compete to thermodynamically adsorb onto the foreign surface, creating a protein corona on their surface [6], [28], [29].

The composition of the corona determines the biological identity of the vector. The adsorption of specific serum fractions (opsonins) acts as a template for receptor recognition by mononuclear phagocytes of the reticuloendothelial system (RES) [32]. This opsonization process triggers phagocytosis, which results in the removal of the nanovehicle from the systemic circulation before passive accumulation in the target tissue can occur [32], [6], [28], [29] . Therefore, it is essential to introduce a surface coating capable of masking the inorganic core. The organic covering must ensure steric repulsion, neutralize the surface charge, confer stealth properties, delay immune identification, and increase the vascular half-life of the system [9].

1.4.2 Albumin as a smart vector

In the field of designing coatings for nanomaterials, the use of endogenous macromolecules presents undeniable advantages over synthetic polymers by virtue of their high biocompatibility and negligible immunogenicity. Among these, serum albumin, the main globular protein in plasma, represents a candidate of choice. Although the final clinical target involves interaction with the human organism (whose plasma is dominated by Human Serum Albumin, HSA), *in vitro* experimentation universally employs Bovine Serum Albumin (BSA) as a model macromolecule. The adoption of BSA has been widely validated by scientific literature owing to its high sequence homology with HSA (approximately 76%) and its marked conformational overlap [3]. This experimental choice guarantees a chemical and biological behavior completely analogous to the human counterpart, while simultaneously offering undeniable advantages in terms of availability, protocol standardization, and cost sustainability. The saturation of the surface with a BSA monolayer acts as a steric shield; the masking of the vector drastically limits non-specific adsorption by opsonins, providing the system with excellent stealth properties that prolong its circulation half-life [33].

The true versatility of BSA as a nanomedical platform lies in its complex three-dimensional architecture, which serves a dual function essential for the development and characterization of nanocarriers. On the one hand, the external surface of the macromolecule exposes a high number of lysine residues [3]. The presence of these free primary amino groups provides ideal nucleophilic sites for covalent anchoring of the protein to the inorganic core, ensuring robust stabilization (**Figure 1.4**). In contrast, the tertiary structure retains specific hydrophobic pockets and internal basic domains. Physiologically responsible for the transport of lipids and metabolites, these non-covalent interaction sites maintain their functionality even when the protein is anchored. This structural characteristic is crucial from a therapeutic perspective, allowing the encapsulation of hydrophobic pharmacological molecules for theranostic applications [33], and is simultaneously responsible for binding with specific analytical dyes used for the spectrophotometric quantification of the vector (e.g., Bradford Assay [34]).

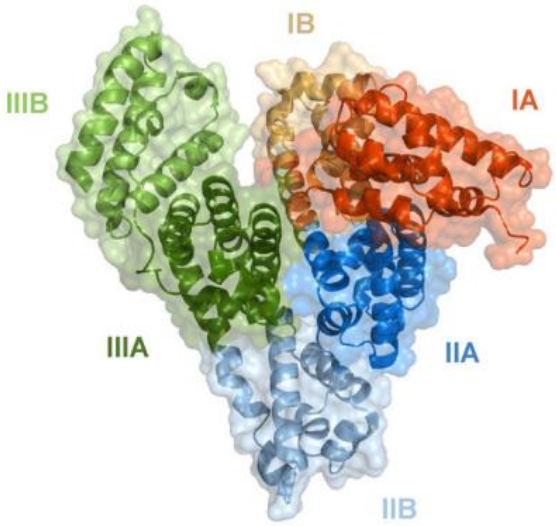


Figure 1.4: Crystallographic structure of BSA. The macromolecule presents a globular conformation consisting of approximately 67% α-helix secondary structures, organized into three main domains. This spatial architecture guarantees the exposure on the external surface of numerous lysine residues (free primary amino groups), which act as essential reactive sites for covalent anchoring to the nanoparticles [3].

In addition to guaranteeing colloidal stability and loading capacity, the BSA coating, acting as a perfect mimetic of human albumin, functioned as a true active ligand [3]. Neoplastic physiology exploits the massive catabolism of plasma proteins to sustain a high tumor proliferative rate by accumulating amino acids. Numerous tumor phenotypes overexpress high-affinity receptors for albumin, including the endothelial receptor gp60, the main mediator of capillary transcytosis, and the glycoprotein Secreted Protein Acidic and Rich in Cysteine (SPARC), abundantly secreted into the extracellular matrix of the tumor microenvironment [33], [34], [35], [36]. Therefore, the protein coating allows the nanoparticles to evade defenses and actively exploit these receptor complexes, promoting a selective endocytosis mechanism that favors the accumulation and intracellular internalization of the nanocarrier [33], [34], [35], [36].

1.4.3 Bioconjugation chemistry: covalent functionalization via carbodiimide chemistry

The *in vivo* efficacy of the protein coating is determined by the stability of the chemical bond that anchors it to the inorganic substrate. The physical adsorption of albumin, although kinetically rapid, is governed by a weak equilibrium. In the bloodstream, hemodynamic shear forces and competition with other plasma molecules lead to rapid desorption of the protein corona [4].

Bioconjugation chemistry relies on covalent cross-linking to ensure complex integrity. The protocol based on the carbodiimide/succinimide system, also referred to as carbodiimide chemistry, represents a robust strategy for the functionalization of nanomaterials [17], [18].

Specifically, the presence of carboxylic groups (-COOH) on the surface of citrate-coated IONPs allows for their covalent functionalization via a carbodiimide-mediated amidation [38], [39]. Amidation consists of a reaction between a carboxylic acid and a

primary amine to form an amide bond; however, the direct interaction between these two functional groups is ineffective due to the low intrinsic reactivity of carboxylic acids. To overcome this limitation, the inorganic surface is reacted with a coupling agent such as 1-ethyl-3-(3-dimethylaminopropyl) carbodiimide (EDC) [39]. This molecule activates the carboxylic terminals, leading to the formation of a reaction intermediate, O-acylisourea. Although capable of reacting with nucleophilic species, this intermediate is unstable in an aqueous environment: in the absence of a timely nucleophilic attack, it undergoes hydrolysis, regenerating the original carboxylic groups and producing an inactive urea derivative.

To increase the coupling efficiency, N-hydroxysuccinimide (NHS) or, as in the case of this study, its water-soluble analog Sulfo-NHS is therefore added to the reaction mixture. This molecule binds to the intermediate via nucleophilic attack, promoting the release of the urea portion of the EDC and leading to the final formation of an activated ester (NHS ester), as illustrated in the general mechanism in **Figure 1.5**. This new intermediate chemical species boasts significantly superior hydrolytic stability while maintaining high reactivity towards nucleophilic sites [39].

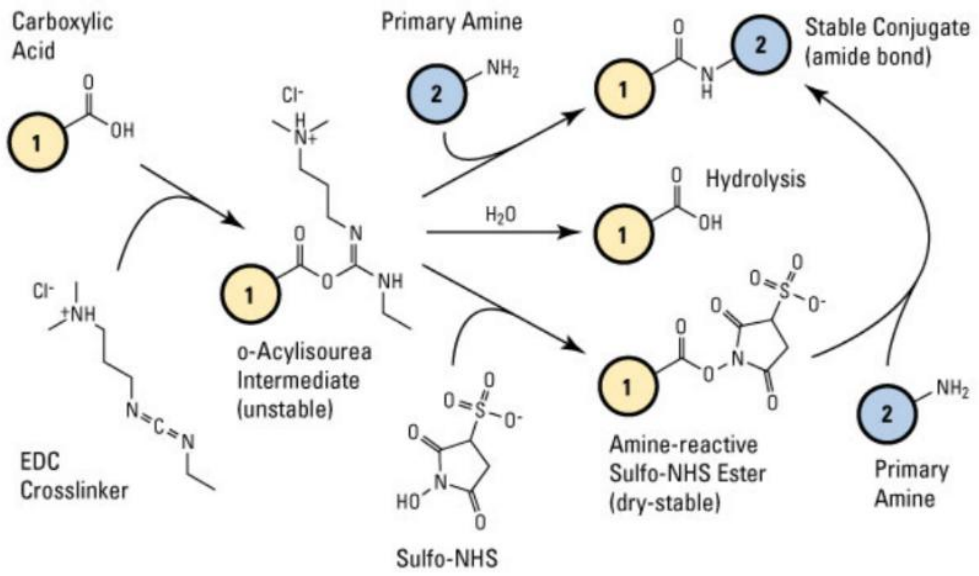


Figure 1.5: Representation of the molecular mechanism of zero-length bioconjugation mediated by EDC/NHS. This process illustrates the preliminary activation of the surface carboxylic group by EDC with the formation of the O-acylisourea intermediate, the subsequent stabilizing transesterification operated by NHS with the release of the urea derivative, and the conclusive nucleophilic attack guided by the primary amines (lysines) of BSA for the generation of the definitive covalent amide bond [38].

The final step of synthesis involves the addition of the target protein macromolecule. The primary amino groups (-NH_2), located on the side chains of the amino acid lysine and exposed on the external conformation of albumin, facilitate nucleophilic attack on the activated ester [39]. This process leads to the formation of a stable covalent amide bond (isopeptidic) that binds the organic shell to the inorganic substrate. This reaction ensures that the coating maintains its structural integrity and receptor directionality, regardless of the physicochemical characteristics of the vascular environment [39].

1.5 Preliminary studies

This thesis is part of a research project oriented towards the development of advanced nanocarriers. The decision to deepen the study of these specific iron oxide-based

formulations originates from the promising results that emerged during previous preliminary studies within the team and the relative biological validations conducted both *in vitro* and *in vivo* [4], [5], [7], [17]. These prior investigations highlighted an excellent safety profile for the use of these architectures, confirming the absence of cytotoxicity, optimal colloidal stability, ideal hydrodynamic dimensions, and excellent biological distribution profiles *in vivo* [4], [5], [7], [17].

To validate their biological safety, extensive multiparametric assays performed on various cell lines (such as Huh7 and HepG2 hepatocytes, EA. hy926 endothelial cells, and MAFs murine fibroblasts) documented efficient cellular internalization without alterations to mitochondrial respiration or activation of apoptotic cascades. Regarding the *in vivo* tests, the nanoparticles, appropriately surface-functionalized with targeting molecules such as bisphosphonates or RGD peptides, have already proven to be effective molecular imaging platforms, allowing for the longitudinal tracking of atherosclerotic plaque evolution in ApoE-/- murine models, the identification of neutrophil infiltration at inflammatory sites, and the mapping of neo-angiogenesis processes in the oncological field [4], [5], [7], [17].

In support of these premises, the research activity conducted in recent years by the group has led to the development of a new generation of iron oxide-based nanomaterials. In particular, extensive screening studies have been conducted to increase the T_1 relaxation time (optimizing positive contrast in MRI), systematically analyzing how Ms varied as a function of the presence or absence of specific doping agents within the inorganic core [5]. The robustness of the synthetic protocol used for the control samples is documented by previous spectrometric investigations: as reported in **Figure 1.6**, the magnetization curves relating to the bare nanoparticles (MW-IONP) confirm the superparamagnetic behavior of the material, showing a total absence of hysteresis at room temperature [4], [5].

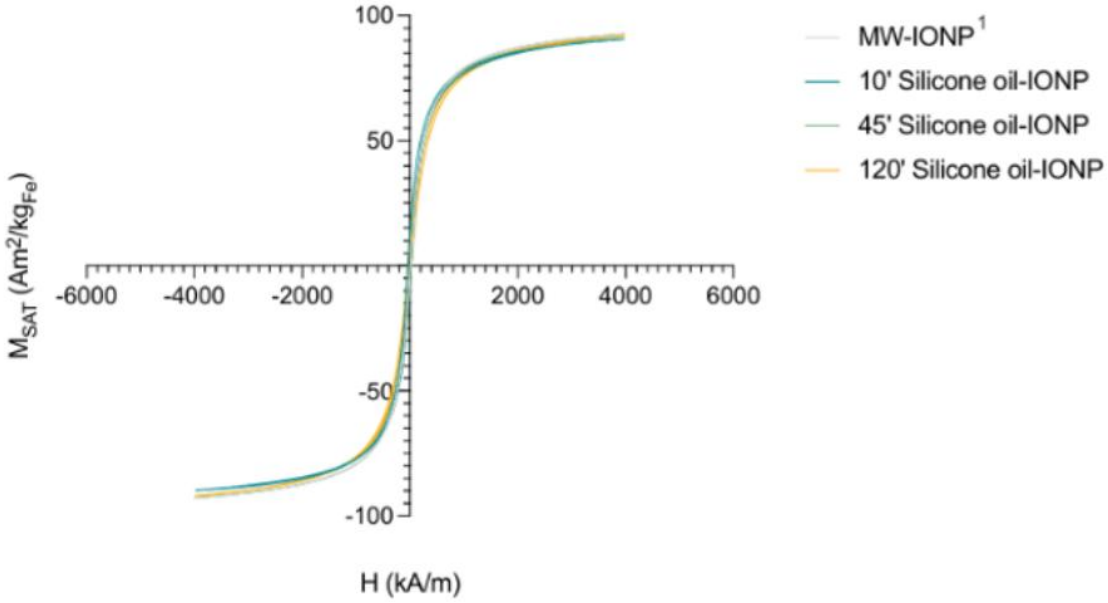


Figure 1.6: Magnetization curves acquired by VSM. The graph illustrates the specific magnetization (expressed in Am²/kgFe) as a function of the applied magnetic field (H, in kA/m) for the control nanoparticles (MW-IONP) and for the formulations synthesized in silicone oil at different reaction times (10, 45, and 120 minutes). The absence of a measurable hysteresis loop (zero coercivity and remanence) confirms the superparamagnetic behavior of the investigated nanosystems at room temperature [4], [5].

These investigations demonstrated the actual advantage of using such agents: the targeted introduction of divalent cations into the crystal lattice significantly improving the overall magnetic behavior of the nanosystem [5]. Consequently, the use of these specific divalent metals represents a strategy of choice to maximize the relaxometric performance of the contrast agent [5].

Building on these premises, this study aimed to explore the extent to which the transverse relaxivity (r_2) of these nanoparticles could be increased while maintaining the structural and chemical properties of the base platform, such as hydrodynamic size, zeta potential, surface chemistry, and behavior in biological models. While previous applications of similar systems mainly focused on vascular imaging, where T_1-weighted

contrast is preferred, T_2 imaging is more suitable for brain applications, particularly for GBM.

Although iron oxide formulations with higher r_2 values are reported in the literature, the goal here was to adapt a known, stable, and biologically validated chemistry for T_2 imaging [5]. To this end, Mg^{2+} and Co^{2+} were selected as doping agents due to their ability to incorporate into the iron oxide crystal lattice [5]. While these ions also provide good T_1 properties, a useful feature for dual-mode imaging, this was not the primary selection criterion.

Rather, Mg^{2+} and Co^{2+} were chosen because they provide adequate r_2 values for this specific class of small-sized samples, which typically exhibit low transverse relaxivity [5]. Therefore, the strategy involved modulating the magnetic properties through the addition of these metals to optimize negative contrast, without altering the overall physicochemical integrity of the nanosystem.

1.6 Objectives

Starting from the premises, the main objective of this project consists of the synthesis, optimization, and in-depth physicochemical characterization of iron oxide nanoparticles doped with specific metal ions. The entire process is aimed at examining relaxometric parameters and conducting direct imaging measurements through MRI phantoms, with the goal of validating their application as high-efficiency dual contrast agents in magnetic resonance. This phase is followed by the development of a nanosystem with real theranostic potential obtained by engineering the surface of an inorganic construct through functionalization with BSA.

To achieve this objective, the experimental plan was divided into a series of operational and analytical steps.

- Synthesize and characterize nanoparticles doped with Mg^{2+} and Co^{2+} ions at increasing concentrations, to analyse their dimensions and the ability to maintain of colloidal stability.
- Quantify the metals incorporated into the lattice by Inductively Coupled Plasma Optical Emission Spectrometry (ICP-OES) analysis and determine their chemical composition by Attenuated Total Reflectance - Fourier Transform Infrared Spectroscopy (FTIR-ATR).
- Evaluate the relaxometric properties of the various formulations, paying particular attention to maximizing the r_2 and optimizing the r_2/r_1 ratio, to then test their real contrast performance through tomographic imaging experiments on phantoms.
- The data of different formulations were cross compared to identify the doping agent and its relative concentration capable of guaranteeing the best magnetic and relaxometric properties.
- Optimize the selected nanoparticle formulation and proceed with its surface coating by engineering it through BSA functionalization. This step aims to confer high colloidal stability and biomimetic properties to the nanosystem, creating a suitable interface for future active targeting studies [3], [33].
- Characterize and quantify the successful bioconjugation, measuring the actual fraction of protein anchored to the nanoparticles utilizing the spectrophotometric Bradford assay [34]. Characterize and quantify the successful bioconjugation, measuring the actual fraction of protein anchored to the nanoparticles utilizing the spectrophotometric Bradford assay. The physicochemical validation of this architecture lays the structural foundations for its prospective use aimed at crossing the blood-brain barrier and the targeted treatment of tumors with high metabolic consumption of albumin, such as glioblastoma [35], [36], [37].

2 Materials And Methods

2.1 Synthesis and Purification of Iron Oxide Nanoparticles

The synthesis of undoped IONPs (control) and variants doped with Mg^{2+} and Co^{2+} ions at final concentrations of 6, 12, and 20 mM was conducted using a hydrothermal method in a final reaction volume of 5 mL (**Figure 2.1**). Unlike traditional methods, this approach involves heating the reagents in a solution within a rigorously sealed environment at high temperatures. These conditions induce the development of high internal pressures, which favor nucleation and promote the formation of IONPs characterized by a high degree of crystallinity and excellent polydispersity. Within this methodological framework, the necessary thermal input for the reaction was provided conventionally, by immersing the vials in a thermostated silicone oil bath (**Figure 2.1**).

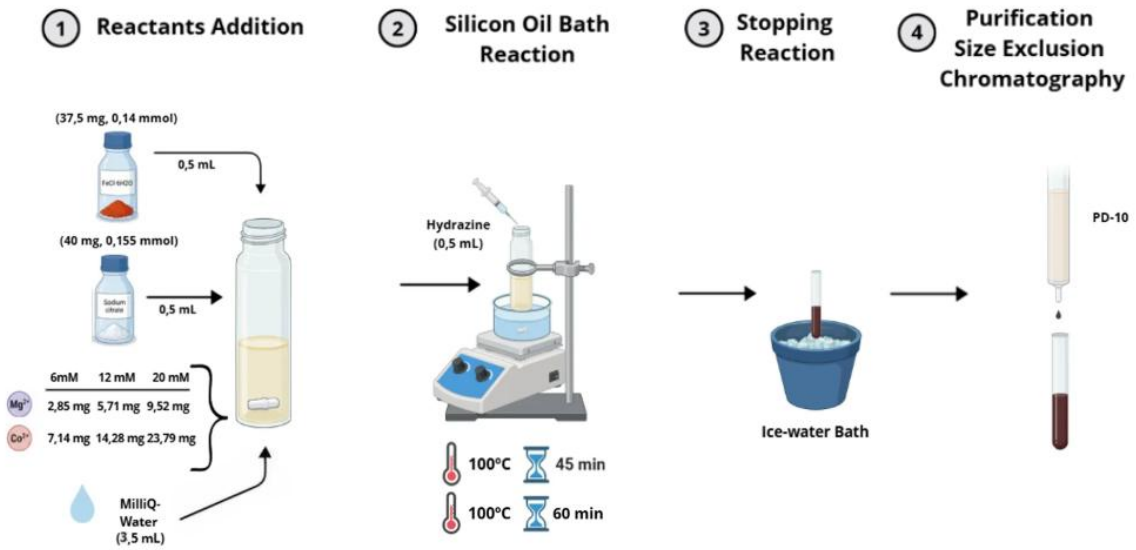


Figure 2.1: Schematic of the synthetic and purification protocol for IONPs. The process is divided into four main phases: (**1**) addition of inorganic precursors and doping agents (Mg^{2+} or Co^{2+}); (**2**) synthesis in a silicone bath at 100 °C with hydrazine injection; (**3**) kinetic blocking of the reaction by means of an ice-water bath; and (**4**) purification by size exclusion chromatography (SEC) using PD-10 columns with elution in Milli-Q water. Figure produced with Biorender.com.

In a G30-type glass vial, equipped with a magnetic stir bar, 0.5 mL of an aqueous solution of ferric chloride hexahydrate ($FeCl_3 \cdot 6H_2O$, Sigma-Aldrich, ACS grade 97.0-102.0%) equal to 37.5 mg (0.14 mmol) and 0.5 mL of sodium citrate 40 mg/mL (0.155 mmol) were mixed in 3.5 mL of Milli-Q water ((**1**) in **Figure 2.1**). Specifically, the synthesis metals and the citrate were introduced at a 1.55:1 ratio. The integration of citrate from this first phase is linked to the need to control the system's interface: the diagnostic and therapeutic performances of IONPs strongly depend on the composition and properties of their surface coating [40]. Since the SPIONs have limited aqueous dispersibility and stability in a physiological environment, surface modification with an organic coating of citric acid is essential to improve biocompatibility, colloidal properties, and biological functionality. In this context, citrate acts as a stabiliser and chelating agent, reducing particle aggregation and making the nanoparticles suitable for subsequent biomedical applications. During the synthesis of the doped samples, to reach the target concentrations, stoichiometric quantities of the respective precursors were added: anhydrous magnesium chloride powder ($MgCl_2$, <200 μm, Sigma-Aldrich, impurities <5%) and cobalt (II) chloride hexahydrate ($CoCl_2 \cdot 6H_2O$, Sigma-Aldrich, ACS grade 98.0-102.0%). Specifically, for concentrations of 6, 12, and 20 mM, 0.03, 0.06, and 0.1 mmol of precursor were added, respectively; in terms of mass, for the magnesium salt this translated to the addition of 2.86 mg (6 mM), 5.71 mg (12 mM), and 9.52 mg (20 mM), and for the cobalt salt to 7.14 mg (6 mM), 14.28 mg (12 mM), and 23.79 mg (20 mM).

The carefully sealed system was immersed in a pre-thermostated silicone bath at 100 °C ((**2**) in **Figure 2.1**), operating constantly under a fume hood. Following thermal stabilization, the reduction reaction was initiated by injecting 0.5 mL of hydrazine hydrate ($N_2H_4 \cdot H_2O$, Sigma-Aldrich, reagent grade 50-60%) into the vessel. Magnetic stirring was maintained for an initial reaction time of 45 minutes, subsequently increased to 60 minutes to optimize the physicochemical properties of the final product. Kinetic

blocking of the reaction (quenching) was induced by rapidly transferring the vial to an ice-water bath ((**3**) in **Figure 2.1**).

To remove unreacted inorganic precursors and residual hydrazine, the suspensions were purified by SEC utilizing pre-packed disposable PD-10 columns (Cytiva), containing Sephadex G-25 resin ((**4**) in **Figure 2.1**). These columns were previously equilibrated with 4 volumes of Milli-Q water. Subsequently, 2.5 mL aliquots of the crude sample were loaded onto each column and pushed into the stationary phase using a 300 μL stacking volume of Milli-Q water. The final elution of the purified nanoparticles was obtained by adding 3 mL of Milli-Q water; the eluted product was finally collected in Falcon tubes for the subsequent functionalization and characterization phases.

2.2 Elemental Analysis by Inductively Coupled Plasma Optical Emission Spectrometry

The iron content and doping ions of Mg^{2+} and Co^{2+} were quantitatively determined using ICP-OES. To guarantee the solubilization of the inorganic matrix, the samples were subjected to a 24-hour acid digestion process based on the use of an *Aqua Regia* mixture. This mixture, composed of nitric acid (HNO_3, Sigma-Aldrich, 70%, purified by redistillation, ≥ 99.999% trace metals basis) and fuming hydrochloric acid (HCl, Sigma-Aldrich, 37%, TraceCERT® for trace analysis) in a 1:1 volumetric ratio, is essential because the former acts as a powerful oxidizing agent capable of degrading the structure of the nanoparticles, while the latter provides chloride ions that stabilize the released metal ions in the form of soluble chlorinated complexes, preventing their precipitation.

Specifically, 200 μL of each acid were added to 100 μL of nanoparticle suspension. At the end of the digestion period, the solution was quantitatively transferred into a volumetric flask, and the reaction vial was repeatedly washed with Milli-Q water to ensure complete recovery of the analyte. The final volume was calibrated to 10 mL. The obtained solution

was stored in Falcon tubes, following a rigorous single-use protocol for pipette tips and plastic instrumentation, to eliminate any risk of cross-contamination between samples.

The quantification was carried out by interpolation of the measured signals against calibration curves constructed with certified standards, thus guaranteeing a precise measurement of the actual molar concentration of iron and the degree of incorporation of the doping metals within the crystalline structure of the nanoparticles.

The samples were sent to the Soil, Plant, and Water Analysis Service of the Institute of Agricultural Sciences (ICA-CSIC), where elemental analysis was performed using a Perkin Elmer Optima 4300 DV instrument.

2.3 Dimensional Analysis and Colloidal Stability

Physicochemical characterization of colloidal properties is fundamental to understanding the behavior of nanoparticles. Dynamic light scattering (DLS) technique allows for the determination of the hydrodynamic diameter, which reflects the dimensions of the core particle, including the solvation layer and the ions closely associated with the surface. The physical principle of DLS is based on the analysis of fluctuations in the intensity of scattered light caused by the Brownian motion of suspended particles; smaller particles move faster than larger ones [23], and the diffusion coefficient obtained allows calculating the hydrodynamic diameter through the Stokes-Einstein equation (**1**):

$$D = \frac{k_B T}{6\pi\eta r} \quad (1)$$

The parameters are defined as follows:

- **D:** diffusion coefficient (m^2/s).
- **k_B:** Boltzmann constant (1.38×10^{-23} J/K).

- **T:** absolute temperature expressed in Kelvin (K).
- **η:** dynamic viscosity of the fluid (Pa·s).
- **r:** hydrodynamic radius.

This measurement is coupled with the determination of the Polydispersity Index (PDI), which provides a dimensionless measure of how broad the particle size distribution is. Analysis of the PDI value defines the degree of sample homogeneity: PDI values below 0.1 indicate a highly monodisperse system characterized by a narrow size distribution; values between 0.1 and 0.4 reflect moderate polydispersity, while values above 0.4 describe polydisperse samples, indicating significant heterogeneity in the sizes of suspended nanoparticles [41].

System stability is evaluated using the Zeta potential. To achieve this, the Smoluchowski equation is typically used (**2**) [25]. This formula is applicable when the thickness of the electrical double layer is very small compared to the particle radius:

$$\zeta = \frac{\mu\eta}{\epsilon} \qquad (2)$$

- **ζ:** Zeta potential (V).
- **μ:** electrophoretic mobility ($m^2 \cdot s^{-1} \cdot V^{-1}$).
- **η:** viscosity of the dispersing medium (Pa·s).
- **ε:** dielectric permittivity of the medium (F/m).

The Zeta potential represents the difference in electrical potential between the slipping plane of the particle and the bulk of the dispersing medium: a high absolute value of the Zeta potential indicates strong electrostatic repulsion that prevents aggregation phenomena [42].

Finally, the measurement of electrical conductivity provides information on the total ionic concentration, which directly influences the behavior of the electrical double layer

[42]. As conductivity increases, the accumulation of counterions around the nanoparticles restricts the thickness of the double layer. Monitoring this parameter is critical, as severe Debye length compression leads to a significant underestimation of the actual surface charge and can prematurely trigger colloidal destabilization during the analysis [42].

The hydrodynamic diameter and surface charge of the nanoparticles were evaluated using DLS and laser Doppler micro-electrophoresis techniques, utilizing the Zetasizer Nano ZS90 instrument (Malvern Instruments). The hydrodynamic diameter was measured by DLS in disposable cuvettes model ZEN0040, using 120 μL of undiluted nanoparticle suspension to minimize alterations in the solvation environment of the particles. Concurrently, for the determination of the Zeta potential, the samples were subjected to a 1:5 dilution in a 1 mM aqueous sodium chloride solution (NaCl, Sigma-Aldrich, BioXtra ≥ 99.5%), used as a supporting electrolyte; the analysis was conducted using specific DTS1070 cuvettes. This physicochemical characterization procedure allowed correlation the average dimensions and colloidal stability of the formulations with the different doping concentrations, providing data related to the structural integrity of the sample.

Specifically, to evaluate the stability of the nanoparticles, both particle size and zeta potential were measured at different time intervals: immediately after synthesis (t_0), the following day (t_1), after five days (t_5), after seven days (t_7), and after fifteen days (t_{15}).

2.4 Fourier Transform Infrared Spectroscopy

FTIR-ATR was used as a structural investigation technique to characterize the molecular fingerprint of the synthesized nanoparticles. The physical principle of the technique is based on the absorption of electromagnetic radiation in the mid-infrared range (typically between 4000 and 400 cm^{-1}), which induces transitions between the vibrational levels

(stretching or bending) of chemical bonds (**Figure 2.2**). Since each bond has its own vibration frequency determined by the atomic masses involved and the force constant of the bond itself, the resulting FTIR-ATR spectrum provides a unique profile, or "fingerprint", of the functional groups present on the surface of the nanoparticles [43].

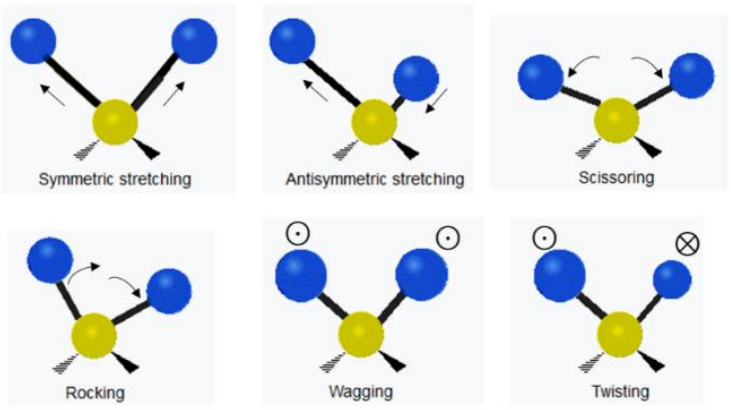


Figure 2.2: Schematic representation of the main molecular vibrational modes involved in the absorption of infrared radiation. Stretching vibrations involve a change in the bond length along its axis, whereas bending vibrations involve a change in the bond angle. These motions are responsible for generating the absorption peaks in the FTIR-ATR spectrum [44].

The FTIR-ATR analysis was conducted to compare the control nanoparticles with the variants doped with Mg^{2+} and Co^{2+} ions at different concentrations. This approach allowed the evaluation of the influence of the dopants on the stability and confirmed the successful functionalization of the nanoparticles with BSA.

Regarding sample preparation, to avoid interference from water absorption bands, a lyophilization step was performed: the suspensions were previously frozen in liquid nitrogen and subsequently subjected to a vacuum drying process (**Figure 2.3**). The measurement was performed using an FTIR spectrometer in Attenuated Total Reflection (ATR) mode, utilizing diamond as the internal crystal for the analysis of the solid sample. After recording the background spectrum to remove environmental noise and verify the

cleanliness of the crystal, the samples were positioned centrally to ensure perfect contact. The spectra were acquired in a range between 4500 and 400 cm^{-1}; subsequently, the data were processed with dedicated software, thus guaranteeing comparability among the different formulations under examination.

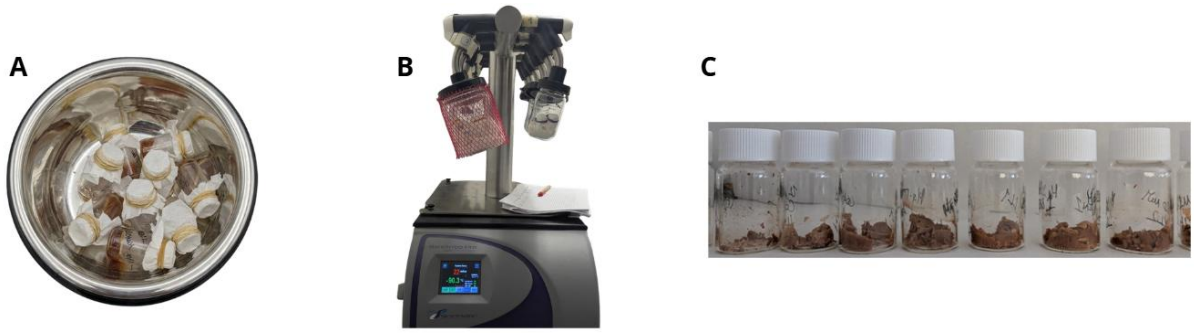


Figure 2.3: Lyophilization steps for FTIR sample preparation. (**A**) Glass vials containing the samples right after freezing in liquid nitrogen. The openings are covered with a breathable material to allow for proper solvent (Milli-Q water) sublimation. (**B**) Primary drying phase. The samples are placed inside glass flasks attached to a benchtop freeze-dryer (BenchTop Pro, SP Scientific). The display shows the operating parameters (pressure and condenser temperature). (**C**) Macroscopic appearance of the final freeze-dried product, showing a solid and porous consistency, ready for analysis.

These analyses were conducted at the Characterization Service of the Institute of Polymer Science and Technology (ICTP-CSIC) using a PerkinElmer FTIR instrument (model UATR Two Spectrometer).

2.5 NMR relaxometry studies

The ability of SPIONs to act as contrast agents in MRI derives from their capacity to locally modulate the magnetic field, accelerating the relaxation of water protons (^1H). The relaxation process is governed by the dipole-dipole interaction between the magnetic moment of the nanoparticles and the nuclear spin of the solvent protons.

According to the Solomon-Bloembergen-Morgan (SBM) theory, the relaxation rate is inversely proportional to the sixth power of the distance between the magnetic center and the proton ($1/r^6$), making IONPs extremely efficient in promoting transverse relaxation thanks to the formation of local field [45], [46].

The NMR characterization was conducted using a 1 T static magnetic field with a 43 MHz Magritek Spinsolve benchtop spectrometer.

To evaluate relaxivity, serial dilutions of each nanoparticle sample in Milli-Q water were prepared directly in 1.5 mL Eppendorf tubes. Four volumetric ratios between water and sample were prepared: 900:100, 925:75, 950:50 and 975:25. After mixing each solution by pipetting or vortex agitation, a 0.5 mL aliquot of each dilution was transferred into NMR tubes for the analysis.

The pulse sequences were configured to determine the relaxation rates R_1 and R_2 ($1/T_1$ and $1/T_2$):

- T_1 measurements: optimized with 4 scans, acquisition time of 0.8 s, and repetition time of 2 s, adapting the Maximum Inversion Time to the sample.
- T_2 measurements: conducted using a CPMG (Carr-Purcell-Meiboom-Gill) sequence with an echo time of 0.5 ms (4 scans, acquisition 0.4 s, repetition 2 s) to minimize the effects of molecular diffusion [31].

For data processing and storage, the NMR signal was integrated using the Spinsolve software, selecting the entire peak for the automatic extraction of the T_1 or T_2 value. Subsequently, to compare the effect of each relaxation time, the r_1 and r_2 factors were calculated as the slope of the linear regression of $1/T_1$ or $1/T_2$ (s^{-1}) as a function of the concentration of Fe and the corresponding metal (Mg^{2+} or Co^{2+}), expressed in mM and determined by ICP-OES.

For data processing and storage, the NMR signal was integrated using the Spinsolve software, selecting the entire peak for the automatic extraction of the T_1 or T_2 value. Subsequently, to compare the effect of each relaxation time, the r_1 and r_2 factors were calculated as the slope of the linear regression of $1/T_1$ or $1/T_2$ (s^{-1}) as a function of the concentration of Fe and the corresponding metal (Mg^{2+} or Co^{2+}), expressed in mM and determined by ICP-OES.

To obtain these relaxivity values (r_1 and r_2), the longitudinal ($R_1 = 1/T_1$) and transverse ($R_2 = 1/T_2$) relaxation rates were plotted against the respective metal concentration $[C]$, according to the linear equation (**3**):

$$R_{1,2} = R_{1,2} + r_{1,2} \cdot [C] \quad (3)$$

where $R_{1,2}$ represents the intrinsic relaxation rate of the diamagnetic background (or solvent), and the slope of the resulting regression line directly corresponds to the relaxivity r_1 or r_2.

2.6 Evaluation of Contrast Efficacy (MRI Phantom)

The efficacy of the nanoparticles as contrast agents for MRI was validated using an experimental phantom, a physical model designed to simulate the behaviour of agents within biological tissues.

SPIONs operate primarily as negative contrast agents because they generate a local magnetic field due to the high magnetic susceptibility of the crystalline core. The field inhomogeneities caused by the nanoparticles accelerate the dephasing of proton spins of the surrounding water molecules, resulting in a shortening of T_2. In MRI images acquired with T_2 -weighted sequences, this phenomenon manifests as a marked signal drop, generating hypointense (dark) areas proportional to the local iron concentration [47].

For the setup of the phantom, sample selection focused on the comparison between two specific formulations: the undoped control nanoparticles (synthesized at 100 °C for 60 minutes) and the variant doped with the maximum concentration of magnesium (IONP 20 mM Mg^{2+}), considered as a representative model to evaluate the impact of the doping metal on imaging performance. Starting from the original purified suspensions, three different dilutions in Milli-Q water were prepared, calculated to obtain final iron concentrations of 1.5 mM, 3 mM, and 8 mM for each of the two sample types. This concentration range was specifically chosen to cover a sufficiently broad dynamic range to accurately map the contrast signal decay curve.

Once prepared and sealed in the appropriate supports, the samples were transferred to the CIC biomaGUNE, which was entrusted with the actual tomographic acquisition. The investigation focused on obtaining T_2 and T_1 weighted parametric maps to quantify image darkening as a function of the molar concentration of iron, providing visual and quantitative validation to support the relaxivity (r_2) data previously measured via low-field NMR relaxometry.

Specifically, the tomographic acquisition was conducted by implementing two distinct protocols to map both the positive and negative contrast effects. For the evaluation of the T1 effect (positive contrast associated with the iron oxide samples, characterized by an increase in brightness with increasing concentration), a strongly T_1-weighted FLASH (SPGR) sequence was selected. The operating parameters included a short repetition time (TR) of 10 ms to saturate the water signal and allow the recovery of the samples' magnetization, combined with a flip angle (FA) of 45° to maximize contrast differentiation. The echo time (TE) was minimized to the instrumental limit of 1.30 ms, as using a longer TE would have erased the signal enhancement due to the rapid decay of T_2* (the effective transverse relaxation time that accounts for both intrinsic molecular relaxation and local magnetic field inhomogeneities) at the maximum concentration of 8

mM. For this sequence, 100 averages (NEX) were set to maximize the signal-to-noise ratio, favoring a FLASH acquisition for its robustness against geometric distortions typical of ultra-short echo time (UTE) sequences.

Concurrently, for the analysis of the T_2 effect (negative contrast associated with the magnesium ferrite, characterized by signal darkening), a multi-slice multi-echo (MSME) or RARE-T_2w spin echo sequence was employed, which is ideal for isolating the true T_2 relaxation by excluding susceptibility artifacts. The protocol utilized a long TR of 3000 ms, necessary to eliminate the T_1 weighting of the buffer, and a TE of 8 ms, an optimized value to generate a clear visual gradient of darkening proportional to the metal concentration. The flip angle was set to 90°/180°, and 20 averages (NEX) were recorded for image reconstruction.

2.7 Functionalization of Nanoparticles with BSA

To improve colloidal stability in biological fluids and confer biocompatibility to the system, magnetic nanoparticles were subjected to a surface functionalization process (**Figure 2.4**), also paving the way for future theranostic applications. This procedure involved the covalent conjugation of BSA to the citric acid coating. EDC/NHS activation chemistry was exploited for the formation of stable amide bonds, followed by a rigorous spectrophotometric quantification of the protein anchored to the inorganic core.

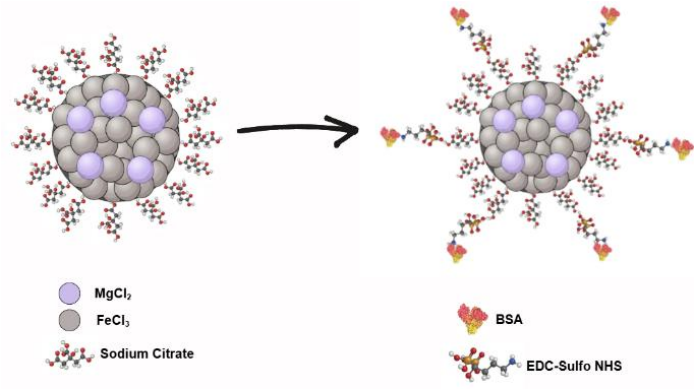


Figure 2.4: Schematic representation of the surface functionalization process showing the final biocompatible nano-complex (BSA IONP 20 mM Mg^{2+}). Figure produced with Biorender.com.

2.7.1 Sample Selection and Synthesis

Based on the results of the structural and magnetic characterization investigations, the entire functionalization process was conducted solely on the variant doped with Mg^{2+} ions at the maximum tested concentration (IONP 20 mM Mg^{2+}).

The synthesis of this formulation was performed, as described in section 2.1, by mixing the iron and magnesium precursors in the presence of sodium citrate. However, in order to prepare the nanoparticles for the subsequent functionalization phase, the final purification phase by SEC (PD-10 columns) was modified compared to the standard procedure: the elution of the nanoparticles did not take place in Milli-Q water, but rather using as mobile phase a 1X phosphate-buffered saline solution at pH 7 (PBS, prepared by dissolving Sigma-Aldrich tablets in Milli-Q water). This precaution allowed us to obtain the starting sample (IONP 20mM Mg^{2+}) directly stabilized in a saline environment.

2.7.2 Buffer Exchange and Carboxylic Group Activation (EDC/NHS)

Activation of the citrate surface carboxylic groups was initiated by adding 12 mg (0.064 mmol) of EDC and 16 mg (0.074 mmol) of NHS (both Sigma-Aldrich). The activation mixture was left to react under moderate orbital agitation for 30 minutes at room temperature (**Figure 2.5**).

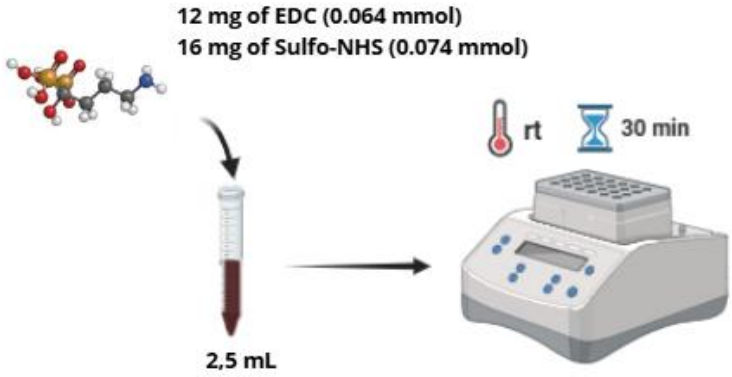


Figure 2.5: Explanatory diagram of the activation process. Figure produced with Biorender.com.

To remove small molecule residues, such as excess EDC and NHS, 2.5 mL aliquots of the suspension in PBS were loaded into Amicon® Ultra-4 centrifugal filters (Merck Millipore) with a Molecular Weight Cut-Off (MWCO) of 30 kDa. Following the activation of the filtration devices by preliminary centrifugation, the samples were purified. After the first filtration, 2.5 mL of 0.1 M HEPES buffer (4-(2-hydroxyethyl)-1-piperazineethanesulfonic acid , Sigma-Aldrich) at pH 8 was added to the retentate. The samples were then centrifuged at 7000 rpm for 3 minutes; this washing and buffer exchange cycle was repeated for three consecutive times. At the end of the procedure, the purified retentate was carefully recovered and resuspended in HEPES buffer, bringing the final volume to 2.5 mL (**Figure 2.6**).

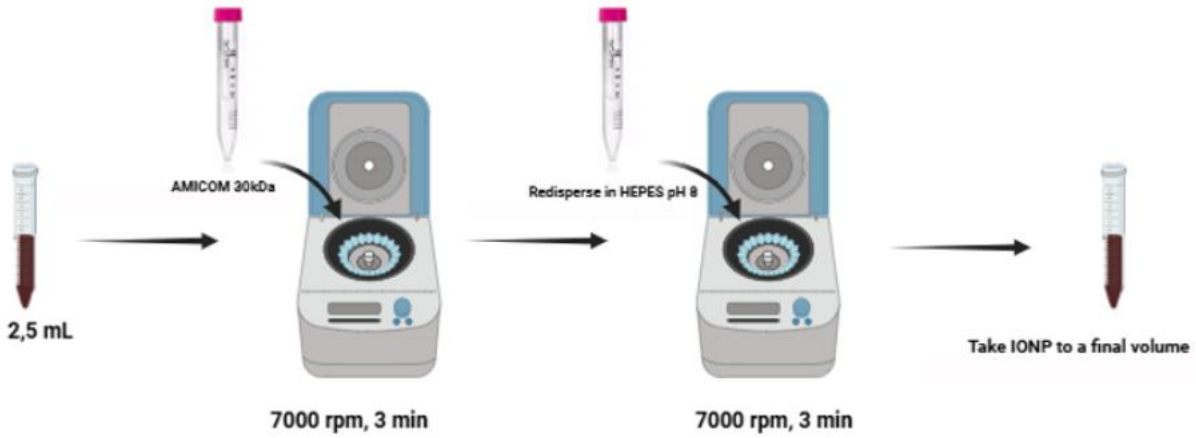


Figure 2.6: Explanatory diagram of the filtration process through centrifugation and resuspension in HEPES buffer. Figure produced with Biorender.com.

2.7.3 Bioconjugation in HEPES and Final Purification in Water

Once the activation process was complete, the conjugation reaction was conducted in one-pot mode. To the activated suspension in HEPES, 200 µg taken directly from a 10 mg/mL stock solution in HEPES were added. The use of HEPES buffer at pH 8 proved essential in this phase: in a slightly basic environment, the primary amines of the lysine residues of the protein are partially deprotonated, maximizing the efficiency of the nucleophilic attack on the succinimidyl ester of the nanoparticles. The mixture was incubated for 1 hour at room temperature under continuous agitation.

At the end of the incubation period, a rigorous purification became necessary to remove the excess unreacted protein, the reaction by-products (e.g., urea), and the HEPES buffer. The suspensions were transferred into new Amicon® Ultra-4 centrifugal filters characterized by a higher cut-off of 100 kDa, which is ideal for the retention of the functionalized nanoparticles and the elution of free BSA (molecular weight ~66 kDa) (Figure 2.7). The washings were performed by adding Milli-Q water and centrifuging at 7000 rpm for 3 minutes, for a total of two complete cycles. The final product, pure and

functionalized, was resuspended in 600 μL of Milli-Q water for subsequent characterization analyses.

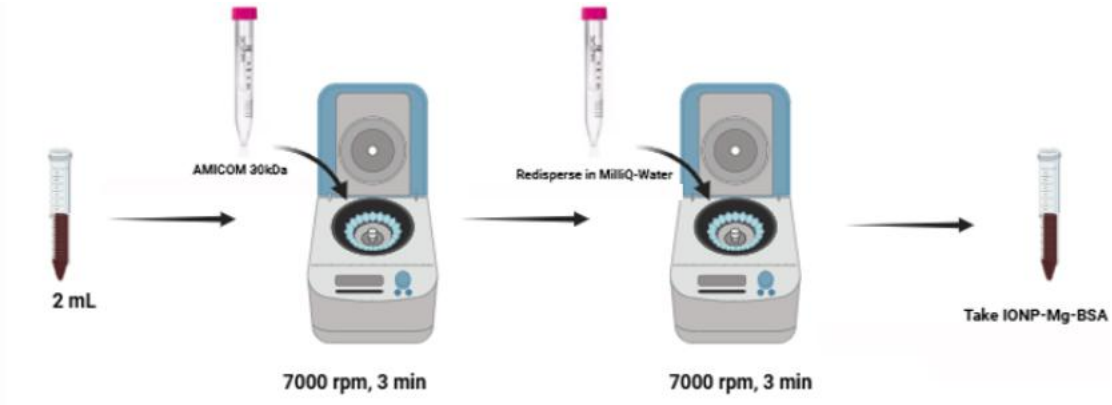


Figure 2.7: Explanatory diagram of the filtration process through centrifugation and resuspension in MILLI-Q water. Figure produced with Biorender.com.

2.7.4 Protein Quantification via Bradford Assay and UV-Visible Spectrophotometry

The effectiveness of the conjugation process was quantitatively evaluated using the Bradford Assay, a widely used colorimetric spectrophotometric method due to its rapidity, ease of execution, and cost-effectiveness.

The theoretical principle of the assay is based on the tinctorial properties of the Coomassie Brilliant Blue G-250 dye [34]. The reagent operates in a distinctly acidic environment: while on one hand this condition prevents its use with poorly acid-soluble proteins and makes it particularly sensitive to the interference of any detergents, on the other hand it allows the free dye to be in its cationic form, characterized by a red-brown color (absorbance peak at 465 nm). When it interacts with the amino acid residues of a protein (through ionic bonds with basic residues such as arginine, and hydrophobic interactions with aromatic residues), the dye undergoes a conformational change that stabilizes it in an anionic form. This interaction causes a shift in maximum absorption

(bathochromic effect) towards 595 nm, imparting a blue color to the solution whose intensity is directly proportional to the protein concentration [34].

From a procedural point of view, the quantification was performed on a transparent 96-well microplate using the commercial Pierce™ Bradford Protein Assay kit (Cat. No. 23200). A critical aspect of this assay is the variability of the colorimetric response (protein-to-protein variation), depending on the amino acid composition of the macromolecule. To eliminate this margin of error, a calibration curve was constructed using the same target protein. Standard dilutions ranging from 25 to 2000 μg/mL were prepared from a 2mg/mL BSA stock solution. The solvent used for the dilutions was the same as the final dispersion medium of the nanoparticles (Milli-Q water), including an analytical blank free of protein.

In the microplate, 5 μL of each analyte (standards or samples) was combined with 250 μL of Bradford reagent. The mixture was homogenized using an orbital shaker for 30 seconds and left to incubate at room temperature for 10 minutes. The samples of suspended functionalized nanoparticles together with their respective filtered washing water were analysed. This step is essential for the indirect quantification of the unreacted protein fraction.

Absorbance was ultimately recorded at 595 nm using the CLARIOstar Plus microplate reader (BMG LabTech). At this wavelength, the monochromatic radiation passes through the sample: a part of the radiation is absorbed by the complex, while the remaining fraction is transmitted to the detector. The relationship between absorbance and analyte concentration is described by the Beer-Lambert law [33] (**4**):

$$A = \log_{10}\left(\frac{I_0}{I}\right) = \varepsilon \cdot l \cdot c \qquad (4)$$

The equation expresses a direct linear proportionality where:

- **A**: absorbance.
- $\boldsymbol{I_0}$ and $\boldsymbol{I}$: the intensity of the incident and transmitted radiation, respectively.
- $\boldsymbol{\varepsilon}$: molar extinction coefficient, a specific constant for each substance at a given wavelength, expressing the probability of the electronic transition occurring.
- **l**: optical path length (the thickness of the cuvette, conventionally equal to 1 cm).
- **c**: molar concentration of the analyte in solution.

In the Bradford assay, the concentration is determined experimentally using the calibration curve prepared with the BSA standards, thus establishing the relationship between absorbance and protein concentration within the linearity range of the method. These values are plotted on a Cartesian plane (concentration on the abscissa, absorbance on the ordinate) and interpolated by linear regression to derive the equation of the line (**5**):

$$y = mx + q \qquad (5)$$

The slope m represents the product $\varepsilon \cdot l$, while the intercept q reflects any background contributions. To cancel the signal deriving from the solvent or reagents, each measurement is preceded by the acquisition of the previously mentioned "blank", namely the solution containing the exact matrix of the sample without the analyte of interest (water). Once the linearity of the method is validated, the obtained equation allows converting the experimental absorbance value of the unknown sample into its actual concentration.

As previously mentioned, the inorganic iron oxide core suspended in water can absorb or scatter light radiation, generating a background signal capable of distorting the concentration estimate. To overcome this bias, in parallel with the functionalized samples, replicates containing "naked" nanoparticles without BSA were set up to act as

a "blank". Specifically, by subtracting the absorbance of this control from the optical signal recorded for the functionalized samples, it was possible to obtain the net value attributable solely to the conjugated BSA.

In order to ensure the statistical validity of the data, each determination was performed in technical triplicate. Finally, the spectrophotometric readings were strictly completed within a 60-minute time window from the addition of the dye, a limit beyond which the chromatic signal loses its thermodynamic stability.

3 Results And Discussion

Developing new contrast agents remains a key factor for investigating pathological mechanisms in preclinical and clinical environments. For MRI applications it is essential, not only to achieve high relaxivity values, but also to ensure reproducible synthesis processes, stable colloidal properties, and safe metabolic clearance. Consequently, a physicochemical characterization was performed to validate the synthesized platforms. The main innovation of these specific formulations is their ability to act as dual T1/T2 contrast agents while maintaining a highly compact hydrodynamic size and colloidal stability. Combining this characteristic in such a dimensionally controlled system represents a distinct technical advantage. Furthermore, the particles were functionalized with BSA. Although albumin is a commonly used approach to extend circulation time and facilitate active targeting, its inclusion here is intended to complete the nanocarrier architecture, establishing a solid baseline for future *in vitro* and *in vivo* theranostic applications.

3.1 Colloidal Stability: Evolution of Hydrodynamic Size and Zeta Potential over time

With the aim of confirming the suitability of the synthesized IONPs for the subsequent functionalization phases, an analysis of their colloidal stability over time was conducted, monitoring the evolution of the hydrodynamic diameter and Zeta potential. In the initial screening phases, aimed at evaluating the impact of the introduction of heterometallic ions within the crystal lattice, the synthesis was conducted in triplicate, adopting a reaction time of 45 minutes. Mg^{2+} and Co^{2+} ions were employed at increasing concentrations (6, 12, and 20 mM) (**Figure 3.1**). Monitoring by DLS, prolonged for 15 days, highlighted profoundly different behaviors depending on the doping metal. The formulations supplemented with cobalt maintained a contained hydrodynamic

diameter (5-10 nm) (**Figure 3.1.A**), resulting perfectly superimposable on the undoped control. In contrast, the formulations containing magnesium showed a dimensional increase proportional to the precursor concentration, reaching an initial hydrodynamic diameter of approximately 20-22 nm for the 20 mM sample (**Figure 3.1.C**).

Reference crystallographic studies (Herraiz et al., 2024 [5]) demonstrate that the substitution of iron with bivalent cations (Mg^{2+} or Co^{2+}) induces a distortion of the unit cell which invariably results in a variation of the crystal volume. Therefore, the dimensional increase recorded by DLS for magnesium is not attributable to a growth of the core, but rather to interface dynamics [5]. The same literature highlights, in fact, a close correlation between the hydrodynamic diameter and the percentage of organic coating effectively anchored to the surface. Cobalt favors a high surface affinity, integrating into the core and maintaining a compact dimensional profile, which translates into a denser citrate coating; this reduces the interaction with water molecules, keeping the hydrodynamic radius contained [5], [40]. Conversely, the lattice strains induced by magnesium alter the surface chemical affinity, resulting in a lower percentage of stabilized citrate. This configuration coordinates a more voluminous hydration layer, directly responsible for the instrumentally measured dimensional increase [5].

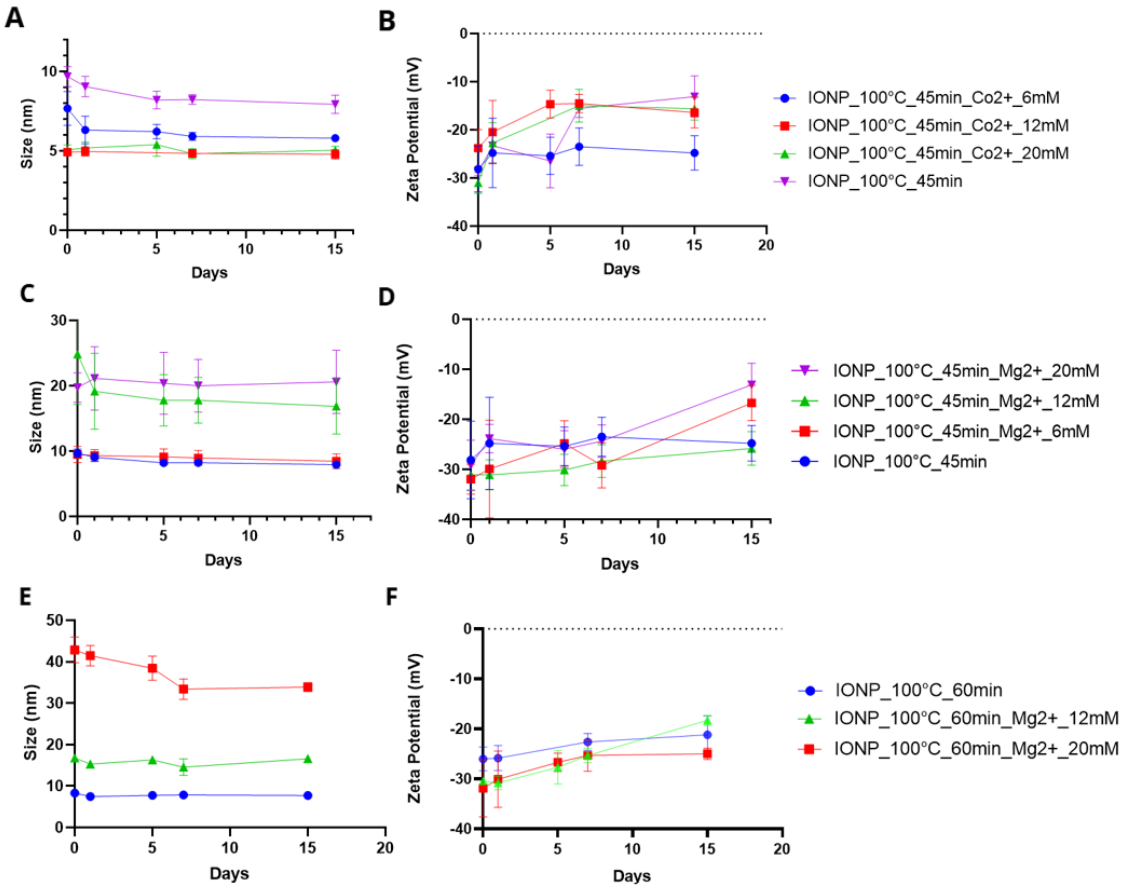


Figure 3.1: Colloidal characterization over time (up to 15 days) of undoped iron oxide nanoparticles (control) and doped with Cobalt ions (Co^{2+}) and magnesium ions (Mg^{2+}) at different concentrations (6, 12, and 20 mM), synthesized at 100 °C for a reaction time of 45 and 60 minutes. (**A**) Trend of the hydrodynamic diameter (Size, nm) measured by DLS for nanoparticles containing ions Co^{2+} at 45 minutes. (**B**) Evolution of the Zeta potential (ζ, mV) measured by laser Doppler micro-electrophoresis for the evaluation of surface stability and electrostatic charge in NaCl suspension for nanoparticles containing Co^{2+} at 45 minutes. (**C**) Trend of the hydrodynamic diameter (Size, nm) measured by DLS for nanoparticles containing ions Mg^{2+} at 45 minutes. (**D**) Evolution of the Zeta potential (ζ, mV) measured by laser Doppler micro-electrophoresis for the evaluation of surface stability and electrostatic charge in NaCl suspension for nanoparticles containing Mg^{2+} at 45 minutes. (**E**) Trend of the hydrodynamic diameter (Size, nm) measured by DLS for nanoparticles containing ions Mg^{2+} at 60 minutes. (**F**) Evolution of the Zeta potential (ζ, mV) measured by laser Doppler micro-electrophoresis for the evaluation of surface stability and electrostatic charge in NaCl suspension for nanoparticles containing Mg^{2+} at 60 minutes. Plots produced using GraphPad Prism 8.

Despite the expansion of the hydrodynamic volume, the data relating to the Polydispersity Index (PDI) reveal that an increase in the Mg^{2+} concentration corresponds to a progressive regularization of the system (**Figure 3.2**). At 45 minutes, the PDI undergoes a clear decrease, passing from the value of approximately 0.30 of the control down to 0.20 for the 20 mM formulation (**Figure 3.2.A**). Although an absolute monodispersity is not configured (typically associated with variations of less than 5%), this trend indicates a marked kinetic control by the doping cation. The increase in magnesium concentration raises the energy of the system, favoring, in accordance with classic models of nanomaterial formation, a "burst" type nucleation event, i.e., a rapid and simultaneous genesis of crystalline seeds [40]. Since the nuclei form at the same instant, they undertake the subsequent growth phase in a synchronized manner; this kinetic control prevents inhomogeneous ripening. This thermodynamic setup, combined with a more homogeneous exposure of the surface anchoring sites for citrate, effectively prevents micro-aggregation phenomena, yielding a highly homogeneous nanoparticle population [5] , [40].

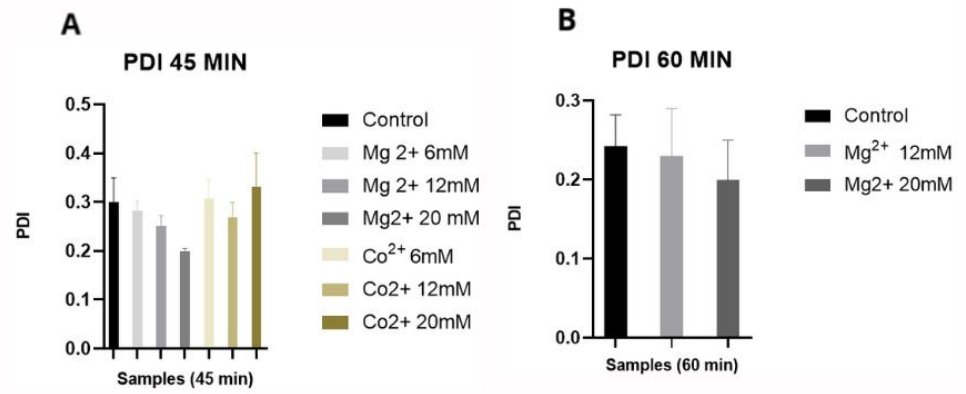


Figure 3.2: Evaluation of PDI for the different nanoparticle formulations. (**A**) PDI values relating to the syntheses conducted for 45 minutes: comparison between the undoped control and the samples doped with magnesium (Mg^{2+}) or cobalt (Co^{2+}) ions at increasing concentrations (6, 12, and 20 mM). (**B**) PDI values relating to the optimized syntheses at 60 minutes: comparison between the control and the samples doped with magnesium ions at 12 and 20 mM. Plots produced using GraphPad Prism 8.

As further confirmation of the structural stability, the Zeta potential values for all syntheses at 45 minutes were maintained in the range between -20 mV and -35 mV (**Figure 3.1.B**, **Figure 3.1.D**), guaranteeing optimal electrostatic repulsion conferred by the exposed carboxylic groups. The first findings emerging from the relaxometry investigations have, however, revealed the need to optimize the protocol to increase the contrast efficiency. For this purpose, the reaction time was extended to 60 minutes. The rationale for this modification lies in the nature of the thermal input employed: the 60 minutes therefore constitute the thermodynamic time frame necessary to allow the citrate to reorganize into a more structured surface coating [5], [40]. The extension of the thermal input entails an inevitable dimensional compromise. In the optimized set at 60 minutes (**Figure 3.1.F**, **Figure 3.1.G**), the IONPs doped with 20 mM magnesium show an initial hydrodynamic diameter close to 42-43 nm (**Figure 3.1.F**), which reaches a stability plateau over the 15 days of monitoring. In the lower affinity system such as magnesium, extending the synthesis time to 60 minutes allows the citrate to reorganize into its most extended form, incorporating a voluminous hydration layer that increases the measured hydrodynamic diameter but as will be analyzed later, optimizes the relaxometry performance. In analogy with the trend observed at 45 minutes, the increase in concentration regularizes the dispersion of the sample, lowering the PDI to 0.20 (**Figure 3.2.B**) and consolidating the Zeta potential at stable values around -32 mV (**Figure 3.1.B**).

3.2 Quantification by Inductively Coupled Plasma Optical Emission Spectrometry

In order to experimentally confirm the effective incorporation of heterometallic ions within the crystal structure and to evaluate the overall yield of the synthetic process, the purified formulations were subjected to elemental analysis by ICP-OES spectrometry. The quantitative results, summarized in **Table 3-1**, initially report the mass content (mg/L) of iron, magnesium, and cobalt measured in the samples.

Table 3-1: The table summarizes the quantitative data extrapolated from the ICP-OES analysis (real concentration in mg/L and mM, heteroatom/iron molar ratio, and percentage incorporation efficiency) of iron (Fe), magnesium (Mg^{2+}), and cobalt (Co^{2+}) determined by ICP-OES spectrometry for the different IONP formulations. The samples are divided based on the hydrothermal synthesis time (45 and 60 minutes at 100 °C). The highlighted row indicates the samples selected for subsequent relaxometry and infrared spectroscopy studies.

	Sample	Metal	mg/L (ppm)	[Concentration] (mM)	Ratio [M]/[Fe]	Incorp. (%)
100°C 45min	Control	Fe^{+3}	10,59	18,96	-	82,17
	Mg2+_6mM	Fe^{+3}	9,44	16,9	0,0487	73,213
		Mg^{+2}	0,2	0,8228		16,6
	Mg2+_12mM	Fe^{+3}	9,86	17,65	0,035	76,65
		Mg^{+2}	0,32	0,617		6,2
	Mg2+_20mM	Fe^{+3}	11,92	21,34	0,0964	92,42
		Mg^{+2}	0,5	2,057		12,3
	Co2+_6mM	Fe^{+3}	11,09	19,86	0,0683	86,06
		Co^{+2}	0,8	1,357		27,13
	Co2+_12mM	Fe^{+3}	10,94	19,59	0,1844	84,84
		Co^{+2}	2,13	3,614		36,13
	Co2+_20mM	Fe^{+3}	8	14,33	0,3067	62,09
		Co^{+2}	2,59	4,395		26,37
100°C 60min	Control	Fe^{+3}	12,61	22,58	-	97,82
	Mg2+_12mM	Fe^{+3}	10,78	19,3	0,567	83,61
		Mg^{+2}	0,11	11		4,53
	Mg2+_20mM	**Fe^{+3}**	**12,64**	**22,63**	**0,839**	**98,05**
		Mg^{+2}	**0,19**	**19**		**4,69**

To fully understand the dynamics governing the relaxometric performances, the raw data were mathematically reprocessed, with the aim of deriving the molar concentration of the metals within the magnetic cores and the relative encapsulation efficiency. The calculation of the real concentration required the application of a dilution factor of 100, multiplying the values returned by the instrument by this volumetric constant. Subsequently, to standardize the data in terms of molarity, the mass concentrations were converted into millimolarity (mM) by dividing them by their respective standard atomic weights: 55.845 mg/mmol for iron, 24.305 mg/mmol for magnesium, and 58.933 mg/mmol for cobalt.

The percentage incorporation efficiency was finally determined by relating the moles of metal effectively incorporated into the final product to the initial moles dissolved in the reaction environment, according to the following equation (**6**):

$$Incorporation\ Efficiency\ (\%) = \frac{Moles\ in\ the\ final\ product}{Initial\ moles\ in\ reaction} \times 100 \qquad (6)$$

Observing the 45-minute synthesis block, the data highlight how iron encapsulation undergoes fluctuations strictly dependent on the nature and concentration of the added doping agent. While in the magnesium formulations the iron yield is maintained at excellent levels (reaching 92.42% in the 20 mM sample), the addition of cobalt ions triggers a structural competition. At dopant concentrations equal to 20 mM, the excessive presence of ions Co^{2+} severely alters the formation of the spinel lattice, causing a drastic collapse of the iron incorporation efficiency, which drops to 62.09%.

Regarding the doping metals, the analysis reveals complex and non-linear insertion dynamics. Although the absolute amount of incorporated metal (expressed in mg/L) increases as the initial precursor concentration increases, the percentage efficiency follows irregular trends. In the case of cobalt, a clear spatial saturation limit of the lattice emerges: the efficiency rises from 27.13% (at 6 mM) up to a peak of maximum integration of 36.13% at 12 mM, to then regress to 26.37% at 20 mM. Beyond this threshold, the excess ions are no longer able to substitute the iron and remain confined in solution.

The chemical affinity of magnesium proves to be profoundly different. The percentage incorporation yields appear globally lower and fluctuating (from 16.6% at 6 mM, with a drop to 6.2% at 12 mM, settling at 12.3% at 20 mM). However, this more contained insertion represents the true strength of magnesium: by not entering into destructive competition with iron, it preserves the integrity of the crystalline architecture.

This structural synergy is confirmed in the results of the 60-minute protocol. The prolongation of the thermal input definitively stabilizes the system: in the Mg^{2+} 20mM sample, iron encapsulation reaches an exceptional yield of 98.05%. The maintenance of a very high iron concentration, combined with the simultaneous and proven encapsulation of magnesium (4.69%), translates into a stable and optimized crystal lattice.

Comparing these doping levels with previous data (Herraiz et al., 2024 [5]), the measured values fit into a consistent framework. The literature has demonstrated that a massive substitution of iron is not necessary to alter the magnetic behavior of the particle; on the contrary, the targeted introduction of divalent cations at low concentrations is thermodynamically sufficient to induce the lattice distortion necessary to maximize transverse relaxivity values (*r2*). Based on this structural balance, the magnesium formulation highlighted in **Table 3-1** guarantees the peak performance of *r2* and was selected as the contrast agent of choice.

3.3 Functional and surface characterization by FTIR spectroscopy

In order to verify the correct formation of the inorganic core, the nanoparticles were analyzed via Fourier transform infrared (FTIR) spectroscopy. The graphs report the transmittance spectra of the bimetallic formulations containing magnesium (Mg^{2+}) and cobalt (Co^{2+}), compared with the respective controls at 45 and 60 minutes (**Figure 3.3**).

Observing the spectral profiles, the first aspect that emerges is the almost perfect superimposability between the curves of the undoped control and those of the samples containing divalent metals. The absence of exclusive or distinct vibrational bands for cobalt or magnesium should not come as a surprise and is justifiable for two fundamental reasons. First of all, as previously quantified by the ICP-OES analyses, the

doping metals are inserted into the lattice in concentrations clearly lower than the majority share of iron; secondly, the stretching vibrations of the Mg–O and Co–O bonds fall precisely in the same low-frequency region typical of the Fe–O bond. Consequently, any signals linked to the doping agents are completely engulfed and masked by the main band of the core. This similarity between the spectra is a positive indicator, since it demonstrates that the insertion of the doping agent or the thermal prolongation at 60 minutes do not alter the integrity or the chemical architecture of the colloidal coating.

Going into the detail of the band assignment, the broad absorption region visible between 3600 and 3300 cm^{-1} is attributable to the stretching of the O–H bond. In the context of our synthesis, this signal does not simply highlight the water adsorbed on the surface but specifically identifies the structural hydroxyl groups (alcoholic and carboxylic) of the citrate.

The confirmation of correct surface engineering lies in the central zone of the graph. Analyzing the interval around 1730–1700 cm^{-1}, a region that classically identifies the C=O bond stretching typical of free or dimeric carboxylic groups, a substantial absence of signal is noted. Instead, two very pronounced absorptions appear at approximately 1590–1600 cm^{-1} and 1390–1400 cm^{-1}, corresponding to the asymmetric and symmetric stretching vibrations of the carboxylate group ($-COO^-$). This dynamic constitutes the chemical proof that the citric acid carboxylic groups have lost the proton to chemically coordinate to the surface metal sites, anchoring the coating to the particle and guaranteeing electrostatic repulsion. To further support this surface architecture, a band is visible in the 1100–1000 cm^{-1} region, linked to the stretching of the C–O–C bonds of the citrate group itself.

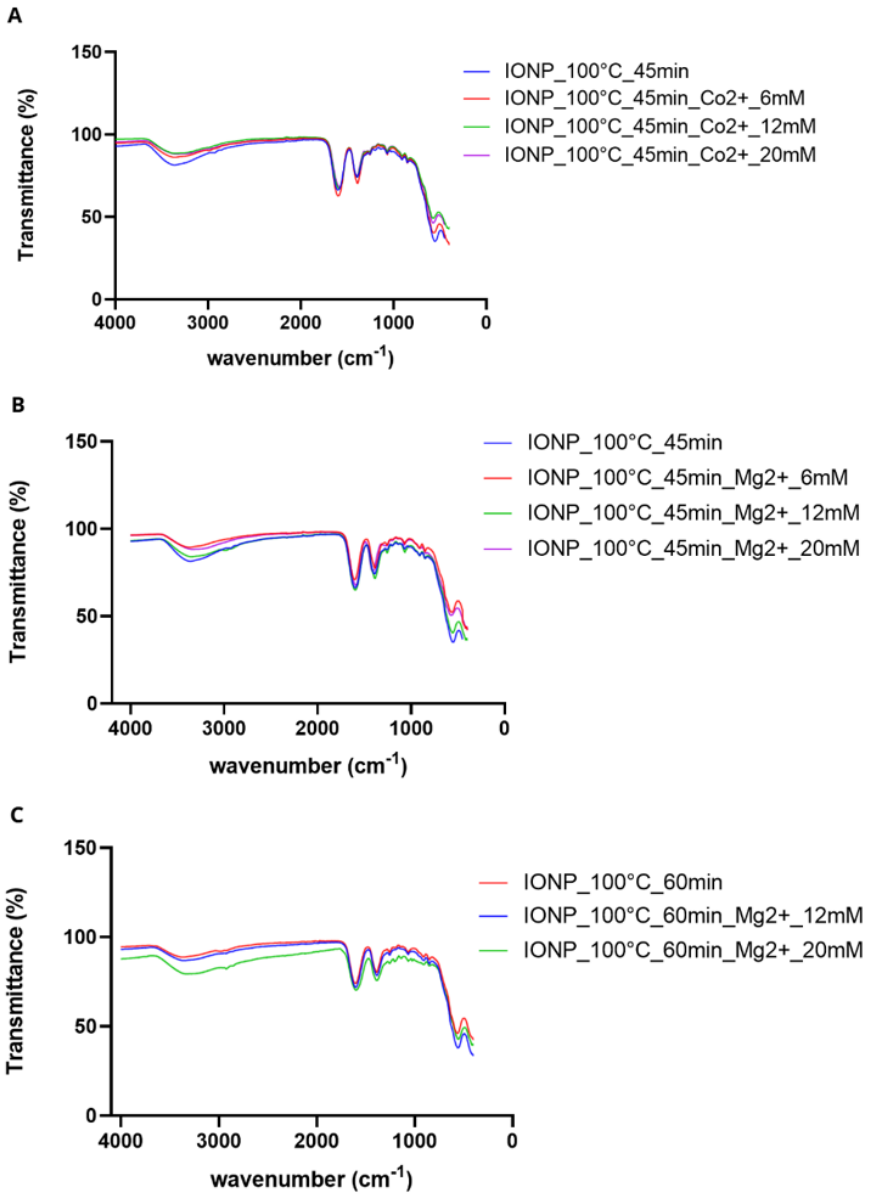


Figure 3.3: FTIR transmittance spectra of nanoparticles. The graphs compare the control formulations with the samples synthesized in the presence of heterometallic cations at increasing concentrations (6, 12, and 20 mM). The top panels (**B, C**) show the effect of magnesium doping for the syntheses conducted at 100 °C for 45 and 60 minutes. The **A** panel illustrates the impact of cobalt doping (synthesis at 45 minutes). Plots produced using GraphPad Prism 8.

Finally, exploring the spectrum below 700 cm^{-1}, an intense peak located at 570–580 cm^{-1} dominates; this signal constitutes the marker of the metal-oxygen (Fe–O) stretching, certifying the correct structuring of the crystal lattice characteristic of the magnetic phase of iron oxide.

3.4 Evaluation of relaxometric properties

The primary objective of the engineering of these nanoparticles is their use as negative contrast agents for MRI. To evaluate this potential, the samples were subjected to relaxometric analysis, calculating r_1 and r_2 , expressed in $mM^{-1}s^{-1}$, derived from the linear regression of the relaxation rates as a function of the total metal concentration (**Table 3-2**). The efficiency of a contrast agent T_2 is strictly linked to its ability to accelerate the dephasing of the proton spins of the surrounding water; therefore, the optimization of the system aims at obtaining high values accompanied by a simultaneous minimization of r_1, in order to maximize the ratio r_2/r_1.

Initially analyzing the 45 minute synthesis set, the data revealed a diametrically opposed behavior depending on the doping metal. Despite the dimensional stability and the lattice incorporation confirmed by ICP-OES analyses, cobalt proved inadequate for optimizing magnetic performance. As clearly seen from the flattening of the regression lines in **Figure 3.4.C** and **Figure 3.4.D**, the introduction of Co^{2+} caused a drastic signal abatement: the *r2* value dropped from 25.52 $mM^{-1}\cdot s^{-1}$ for the control down to a minimum of 2.01 $mM^{-1}\cdot s^{-1}$ for the 20 mM formulation.

This decay in relaxometric properties finds a solid physico-chemical justification in the interface dynamics. As demonstrated by Herraiz et al. (2024) [5], [40], the insertion of cobalt into the inorganic lattice promotes a dense and tight chemical anchoring of the citrate. Although this configuration ensures rigorous control over the hydrodynamic diameter, an excessively compacted organic coating acts as a steric shield. This physical

barrier keeps water molecules at a greater distance from the magnetic core, hindering their free access. Since the dipole-dipole magnetic interaction, which is directly responsible for the proton relaxation mechanism, decays rapidly as distance increases, the high coating density promoted by cobalt effectively nullifies the contrast transfer efficiency to the aqueous environment. This structural limitation led to the definitive exclusion of this metal as a candidate for the subsequent phases of the project.

Table 3-2: Relaxometric parameters of the superparamagnetic nanoparticle formulations synthesized at 100 °C. The table reports the values of specific longitudinal and transverse relaxivity, expressed in $mM^{-1}s^{-1}$, together with the dimensionless ratio r_2/r_1 calculated for each formulation. The data are divided based on the thermal reaction time (45 and 60 minutes) and compare the undoped control samples with the formulations doped with magnesium and cobalt ions at increasing concentrations (6, 12, and 20 mM). The specific values were analytically extrapolated from the slopes of the linear regression lines of the respective relaxation rates as a function of the total metal concentration.

	Sample	r1 ($mM^{-1}\cdot s^{-1}$)	r2 ($mM^{-1}\cdot s^{-1}$)	r2/r1
100°C 45min	Control	10,7211	25,529	2,38
	Mg2+_6mM	7,5597	17,0247	2,25
	Mg2+_12mM	8,0121	27,742	3,46
	Mg2+_20mM	5,9188	28,1884	4,76
	Co2+_6mM	3,9934	8,6467	2,17
	Co2+_12mM	0,9312	2,5629	2,75
	Co2+_20mM	0,9145	2,0198	2,21
100°C 60min	Control	9,3946	20,8844	2,22
	Mg2+_12mM	9,4535	30,8392	3,26
	Mg2+_20mM	**7,9134**	**48,6598**	**6,15**

In contrast, the use of magnesium showed significant potential from the early stages. In the 45-minute protocol (**Figure 3.4.A**, **Figure 3.4.B**), the increase in doping induced a noticeable improvement in transverse efficiency. The 20 mM formulation exceeds the control by recording a of 28.19 $mM^{-1}s^{-1}$ and, an even more relevant finding, doubles the ratio r_2/r_1, bringing it from 2.38 to 4.76. The origin of this improvement lies in the interface dynamics: in agreement with the crystallographic studies by Herraiz et al. [5], the distortion of the inorganic lattice induced by magnesium alters the surface affinity, laying the chemical foundations for a different distribution of the organic coating.

The definitive performance leap, however, is recorded by applying the optimized protocol at 60 minutes (**Figure 3.4.E**, **Figure 3.4.F**). By extending the thermal reaction time, the citrate is provided with the thermodynamic energy necessary to reorganize around the surface distorted by magnesium, forming a significantly thicker and more structured coating. This coating architecture acts directly on the proton relaxation mechanisms [5], [40]. On the one hand, the dense shell shields the magnetic core, limiting the access of water molecules to the inner coordination sphere; this phenomenon physiologically depresses the longitudinal relaxivity, causing the r_1 to drop to 7.91 $mM^{-1}s^{-1}$. On the other hand, the thick hydrated layer drastically slows down the diffusion of water molecules in the outer sphere: the protons remain for a prolonged time under the influence of the local magnetic field, undergoing accelerated dephasing.

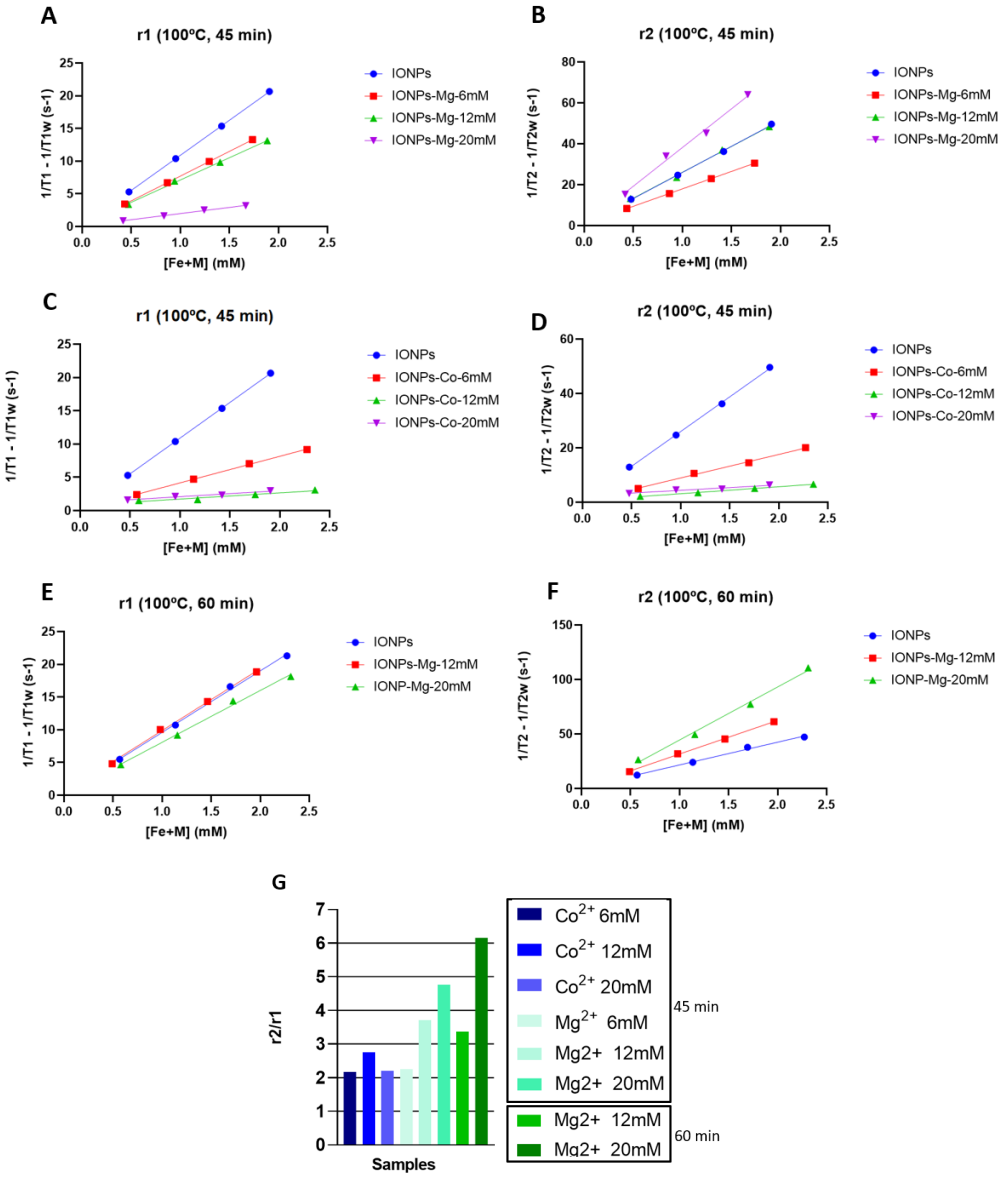


Figure 3.4: The graphs illustrate the linear regressions of the longitudinal $(1/T_1 - 1/T_{1w})$ and transverse $(1/T_2 - 1/T_{2w})$ relaxation rates as a function of the total metal concentration ($[Fe + M]$, expressed in mM), from whose slopes the respective values of specific relaxivity and were extrapolated. Specifically, panels (**A**) and (**B**) show the trend of the relaxation rates for the 45-minute synthesis set, comparing the control IONPs with those doped with magnesium at increasing concentrations (from 6 to 20 mM). Panels (**C**) and (**D**) report the effect of cobalt doping, maintaining the same synthesis time at 45 minutes. Panels (**E**) and (**F**) illustrate instead the results for the formulations synthesized at 100 °C for 60 minutes with magnesium. Finally, panel (**G**) presents a summary histogram of the ratio r_2/r_1 all the analyzed samples. Plots produced using GraphPad Prism 8.

The outcome of this chemical-physical synergy establishes the clear superiority of magnesium at 60 minutes: the regression line assumes the maximum slope of the set, with a r_2 calculated equal to 48.66 $m\mathrm{M}^{-1}\mathrm{s}^{-1}$. The magnetic efficiency of this formulation is moreover supported by absolute instrumental readings, which for the 20 mM samples go as far as to record a remarkably high transverse relaxation rate, equal to 111.11 s^{-1} (**Table 3-3**). The targeted reduction of and the concomitant maximization r_2 of project the ratio r_2/r_1 to the remarkable value of 6.15 (**Figure 3.4.G**).

Table 3-3: Absolute values of the relaxation times and rates instrumentally recorded for the optimized IONP Mg^{2+} 20 mM formulation synthesized at 60 minutes. The table summarizes the T_1 and T_2 relaxation times, expressed in milliseconds, with the corresponding absolute relaxation rates (R_1 and R_2, expressed in s^{-1}) measured at different sample dilutions.

IONP_100°C_60min_Mg^{2+} H_2O : NPs	T1	R1	T2	R2
900 : 100	0,054	18,484	0,009	111,111
925 : 75	0,068	14,749	0,0127	78,740
950 : 50	0,105	9,524	0,02	50,000
975 : 25	0,200	5,000	0,0373	26,810

These relaxometric results represent the final piece of the inorganic optimization process. Although the IONP Mg^{2+} 20 mM formulation at 60 minutes entails an inevitable dimensional compromise in terms of hydrodynamic diameter, the superiority of its magnetic properties certifies the capacity of the nanosystem to generate a highly selective and efficient T_2 contrast, confirming it as the ideal and definitive candidate for the subsequent phase of theranostic engineering by functionalization with BSA.

3.5 Tomographic Evaluation on Phantoms (7 T MRI)

The experimental investigation conducted on the phantoms allowed for outlining a picture of the contrast performance of the nanoparticles. Through an MRI scanner operating at a high magnetic field (7 T), it was possible to acquire tomographic images.

Observing the first row of **Figure 3.5**, relating to the analysis in r_1 and corresponding to the tubes containing undoped IONPs, a progressive increase in signal brightness is noted, which is proportional to the increase in the iron amount. The second row, dedicated to the samples containing Mg^{2+}, shows a similar trend: increasing the metal concentration corresponds to an increase in signal intensity. In accordance with what was theoretically hypothesized for this specific class of materials, the brightness level expressed by the variant doped with Mg^{2+} ions is slightly lower compared to that generated by the control nanoparticles.

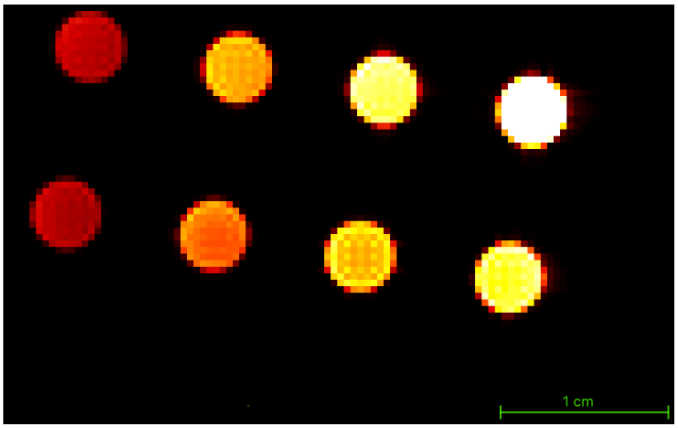


Figure 3.5: Tomographic acquisition weighted in T_1 (FLASH sequence at 7 T) for the evaluation of the relaxivity effect r_1 at different Fe concentrations arranged from left to right: Milli-Q water, 1.5, 3, and 8 mM Fe.

The results of the MRI examination take on greater significance when analyzing the results relating to the r_2 relaxivity, a key parameter for the use of these systems as dual contrast agents (**Figure 3.6**).

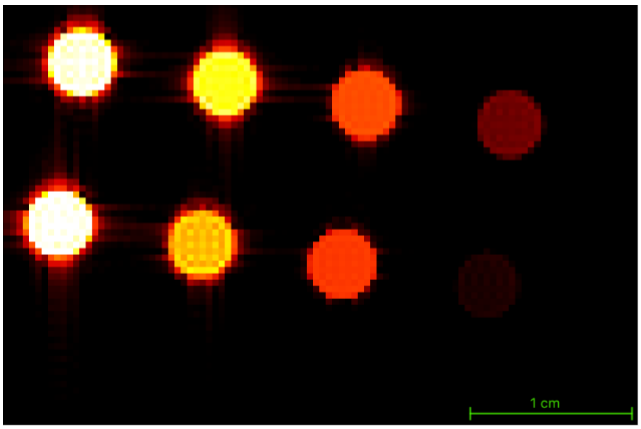


Figure 3.6: T_2-weighted tomographic acquisition (FLASH sequence at 7 T) for the evaluation of the relaxivity effect r_2 at different Fe concentrations arranged from left to right: Milli-Q water, 1.5, 3, and 8 mM Fe.

Analyzing the first row of **Figure 3.6**, relative to the control nanoparticles, the increase in iron concentration translates into a gradual darkening of the signal, typical of the latter. The formulation containing Mg^{2+}, based on the increase in iron and Mg^{2+} concentration, induces a more pronounced signal reduction compared to the control nanoparticles. Under equal conditions, the variant containing Mg^{2+} ions appears visibly darker. This significant increase weighted in r_2 represents the achievement of the set objective; it unambiguously demonstrates that the synthesis process allowed for obtaining nanoparticles capable of simultaneously providing a positive contrast in T_1 and a negative one in T_2.

3.6 Outcomes of functionalization via BSA

The quantification of the BSA protein bound to the nanoparticles was conducted by directly analyzing the resuspended pellet using the Bradford assay.

Primarily, to ensure that the absorbance values fell within the linear range of the calibration line $y = 0.2536x + 0.0081$ with a coefficient of determination $R^2 = 0.9984$ (**Figure 3.7**) and, at the same time, to cope with the reduced amount of BSA and avoid

excessive sample dilution, an optimization work was carried out with the aim of reducing the final resuspension volume to 0.6 mL.

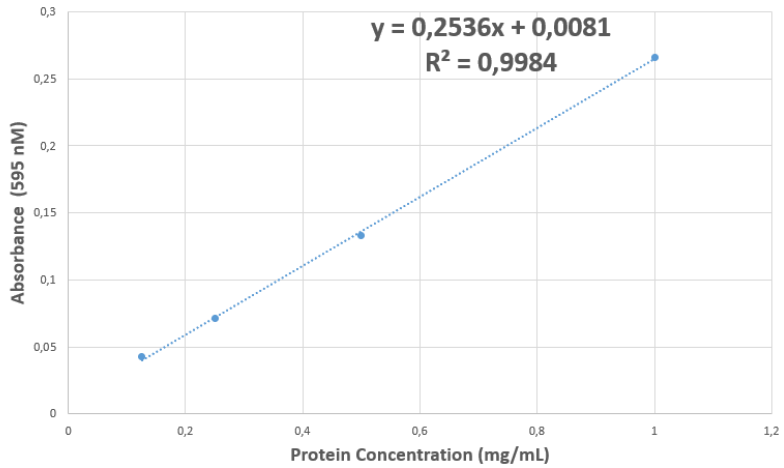


Figure 3.7: Standard calibration curve for protein quantification via the Bradford colorimetric assay. The graph illustrates the linear correlation between the absorbance, measured with a spectrophotometer at a wavelength of 595 nm, and the known concentration of the standard protein (in mg/mL). The interpolation of the experimental data generated the equation line $y = 0.2536x + 0.0081$, characterized by a coefficient R^2 equal to 0.9984.

By calculating the Encapsulation Efficiency (EE%, where the parameter is obtained by directly measuring the protein mass anchored to the nanoparticles, compared to the total mass of BSA introduced at time zero) from the data collected at the end of the first analysis (**7**), it can be seen that the sample chemically activated with EDC/NHS shows a significant yield, close to 76% (**Table *3-4***). In parallel, the sample treated with BSA alone also recorded a high encapsulation, equal to 46.43% of the provided protein. This latter parameter indicates a marked inclination of the protein to adhere to the inorganic surface through weak bonds, such as Van der Waals forces and electrostatic interactions, typical in a physisorption process (**Table *3-4***).

$$EE\% = \frac{\text{Mass of bound protein}}{\text{Total initial protein mass}} \times 100 \qquad (7)$$

Table 3-4: Summary of the nanoparticle functionalization data with BSA over time (0, 6, and 24 hours). For the three analyzed formulations (control, physisorption with BSA alone, and covalent activation with BSA+EDC/NHS), the measured protein concentration ([]BSA, mg/mL), the Encapsulation Efficiency, and the absolute mass of bound protein (mg) are reported. The abbreviation N.D. (Not Detectable) indicates an absorbance below the detection limit of the instrument, confirming the absence of bound protein; consequently, the wording N.A. (Not Applicable) indicates the mathematical impossibility of calculating the %EE starting from a zero protein mass.

	Mg^{2+}			
	IONP (Control)	IONP+BSA	IONP+BSA+EDC_NHS	
[]BSA	N.D.	0,15	0,25	zero-hours
%EE	N.A.	46,43	75,83	
mg BSA	N.D.	0,09	0,15	
[]BSA	N.D.	0,14	0,24	6h
%EE	N.A.	41,90	72,97	
mg BSA	N.D.	0,08	0,14	
[]BSA	N.D.	N.D.	0,07	24h
%EE	N.A.	N.A.	21,45	
mg BSA	N.D.	N.D.	0,04	

The stability tests performed at 24h show the effective retention of the system. This extended timing was made necessary to complete the numerous washing cycles and repeated centrifugations required to purify the sample. This process served to remove the non-covalently bound albumin; thanks to the combined action of the mechanical stress during centrifugation and the effect of the washes in an aqueous environment, the removal of the adsorbed protein in the unactivated control was favored, bringing its yield to 0%, with absorbance values completely superimposable on the blanks. In the activated sample, on the other hand, the efficiency stabilized at 21.4% (**Table 3-4**). This substantial difference demonstrates that using cross-linking agents becomes necessary to overcome the reversibility of weak bonds and create covalent amide bonds resistant to the various washing cycles.

This 21.4% final yield, if converted into absolute mass, allows for evaluating how much of the protein introduced into the formulation is covalently retained on the nanoparticle.

Starting from 200 µg of BSA, the protein fraction anchored to the nanoparticles corresponds to approximately 42-43 µg. This amount, although reduced, provides a chemical-physical explanation regarding the results obtained during the infrared analysis (**Figure 3.8**).

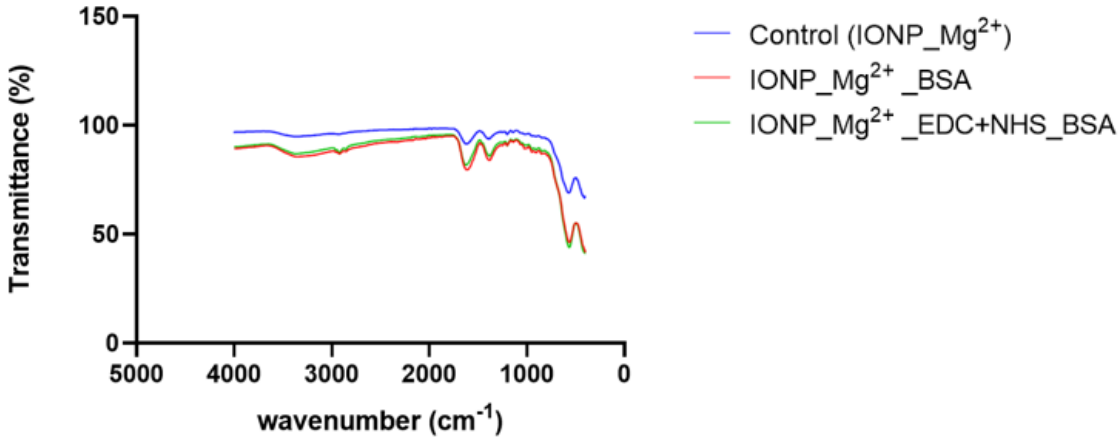


Figure 3.8: FTIR transmittance spectrum of iron oxide nanoparticles Mg^{2+} (60 min) functionalized with BSA and respective controls. Plots produced using GraphPad Prism 8.

Observing the spectra of the functionalized samples (**Figure 3.8**), it is noted that the vibrational bands of amides I, II, and III are not visible, and the profile of the trace follows that of the control nanoparticles. The absence of these signals is due to an instrumental sensitivity limit rather than a failure of the functionalization. The approximately 43 µg of organic matrix indeed constitute a minimal weight percentage compared to the inorganic core. The massive absorption generated by the iron (with a fingerprint in the region below 1000 cm^{-1}) obscures the signal of the thin protein layer located on the surface. The data obtained from the Bradford assay therefore confirm the successful covalent conjugation, highlighting how the amount of protein is, however, below the optical detection threshold for the FT-IR technique.

4 Conclusions

The objective of this thesis work was focused on the design, optimization, and chemical-physical and functional characterization of superparamagnetic iron oxide nanoparticles with the aim of validating their efficacy as advanced contrast agents for magnetic resonance imaging and as vectors for future applications in theranostic nanomedicine. The experimental path pursued allowed demonstrating how the engineering of the inorganic core through targeted doping with divalent ions constitutes an effective strategy to modulate the magnetic properties of the system. Specifically, the initial screening highlighted how the introduction of cobalt (Co^{2+}), while guaranteeing a complete incorporation and high dimensional stability, determines a decay regarding the magnetic performances, making the formulation unsuitable for diagnostic use. Conversely, doping with Mg^{2+} ions proved to be the optimal choice. The optimization of the hydrothermal synthesis protocol, extended to 60 minutes of reaction at 100 °C with a Mg^{2+} concentration equal to 20 mM, allowed for obtaining nanoparticles characterized by a stable hydrodynamic diameter (albeit of approximately 40 nm) and a low polydispersity index. As confirmed by ICP-OES analyses, this specific thermodynamic condition guaranteed a balanced insertion of magnesium within the crystal lattice and, at the same time, an iron encapsulation efficiency equal to 98%. All this translated into an enhancement of the relaxometric performances; the optimized sample recorded an r_2 close to 49 $mM^{-1} \cdot s^{-1}$ and a ratio r_2/r_1 higher than 6, effectively triplicating the efficiency of the undoped control.

The numerical data reported above found visual confirmation in the tomographic acquisitions on phantoms at 7 T. The T_2-weighted images demonstrated the superior capacity of the doped formulation in generating a marked negative contrast, proportional to the concentration of the inserted metal. However, the most relevant clinical aspect that emerged from this validation is the preservation of an excellent positive contrast also in the T_1-weighted acquisitions. It is precisely this performance

balance that closes the conceptual circle of the project: the validation of a highly versatile nanosystem, capable of operating as a dual platform (T_1/T_2) for magnetic resonance imaging.

Subsequently, the second phase of the project aims at the possibility of converting this contrast agent into a theranostic platform by exploiting the surface functionalization with Bovine Serum Albumin (BSA). The use of carbodiimide activation chemistry allowed overcoming the intrinsic thermodynamic instability of simple physisorption. Quantitative investigations demonstrated that, following repeated cycles of centrifugation and washing (monitored up to 24 hours), the system is able to covalently retain over 21% of the initially introduced protein. Although the reduced absolute mass of this organic matrix (approximately 43 μg) made it impossible to confirm the presence of covalent bonds through the qualitative FTIR detection of the amide bands due to the optical masking generated by the ferrite core. The resistance of the coating to washes quantitatively certifies the success of the covalent cross-linking.

In conclusion, the integration of a targeted magnesium-based doping within an iron oxide core, combined with biomimetic surface engineering, allows generating stable nanosystems. These vectors, combining excellent diagnostic properties in MRI with a biologically reactive surface, lay concrete foundations for the development of targeted oncological therapies.

5 Future Perspectives

The results obtained in this study represent the starting point for a series of future developments aimed at optimizing the nanoplatform and investigating its biomedical potential in preclinical models, with reference to the treatment and imaging of glioblastoma multiforme (GBM).

5.1 Dimensional and synthetic optimization

Although the optimized formulation yielded excellent transverse relaxivity (r_2) values, its hydrodynamic diameter is currently oversized to ensure efficient biodistribution and facilitate the crossing of the blood-brain barrier (BBB), a fundamental requirement in neuro-oncology.

To overcome this obstacle, which is related to the initial particle size (approximately 40 nm), the synthesis composition was modified by increasing the amount of sodium citrate. By varying the Metal:Citrate molar ratio, the addition of a larger amount of stabilizing agent was exploited to finely control the nucleation and growth processes, thereby reducing the inorganic core size to approximately 15-20 nm.

5.2 Advanced structural and morphological characterization

In order to understand the structure of the formulated nanoparticles, morphological characterization using transmission electron microscopy (TEM) and scanning transmission electron microscopy (STEM) will be required. Specifically, the use of the HAADF-STEM (High-Angle Annular Dark-Field) technique will be fundamental because this high-resolution investigation will allow for the distinction of the heavier dopant atoms from the lighter elements of the lattice. Thanks to this approach it will be possible to obtain a precise elemental mapping of the inorganic core, independently of the hydrodynamic shell's steric hindrance. These data will be integrated with X-ray

diffraction (XRD) analyses to study the crystal structure. Vibrating sample magnetometry (VSM) will be used to determine the saturation magnetization and thermogravimetric analysis (TGA) to quantify the mass of the organic coating.

5.3 Stability studies and active functionalization

To evaluate long-term stability, the synthesized nanosystem requires incubation in biologically relevant fluids such as DMEM (Dulbecco's Modified Eagle Medium) and FBS (Fetal Bovine Serum). Specifically, DMEM is a basal medium that provides essential nutrients by mimicking the physiological environment, while FBS is a supplement in *in vitro* cultures to provide proteins and growth factors. The analysis consists of monitoring the variations of the hydrodynamic size and Zeta potential at both room temperature and physiological temperature (37 °C).

For subsequent *in vivo* applications, the use of albumin-based nanoparticles is necessary to improve the biodistribution of therapeutic agents. Since one of the primary challenges in using IONPs for the theranostics of central nervous system tumors lies in their limited penetration across the blood-brain barrier, surface engineering will employ advanced functionalization strategies. In this regard, a method of choice involves the use of bioorthogonal chemistry via the reaction between *trans*-cyclooctene (TCO) and tetrazine (Tz), which has proven particularly suitable for obtaining stable covalent bonds and preserving stable colloidal dispersions. The aim of this covalent functionalization with BSA is to improve the pharmacokinetic properties of the vector, promoting its accumulation at the tumor site. Subsequently, this biomimetic coating will serve as an anchor for further ligands (such as triphenylphosphine derivatives) in order to promote active subcellular targeting towards mitochondria.

5.4 Preclinical validation for glioblastoma: *in vitro* and *in vivo*

The efficacy of the engineered platform must ultimately pass through a rigorous biological validation process. *In vitro*, cytotoxicity, biocompatibility, and therapeutic efficacy at different dosages will be evaluated using advanced 3D glioblastoma cell models. The vector's potential ability to reach the brain compartment will be tested through the PAMPA (Parallel Artificial Membrane Permeability Assay), an *in vitro* model used to measure the passive permeability of compounds across an artificial lipid membrane that simulates the blood-brain barrier.

The final goal of the project will involve the translation to *in vivo* animal models, in order to outline the nanocarrier's actual biodistribution profile and perform real-time MRI acquisitions, definitively confirming the applicability of these nanoparticles as next-generation tracers and theranostic agents.

Bibliography

[1] J. Shi, P. W. Kantoff, R. Wooster, and O. C. Farokhzad, 'Cancer nanomedicine: progress, challenges and opportunities', *Nat. Rev. Cancer*, vol. 17, no. 1, pp. 20–37, Jan. 2017, doi: 10.1038/nrc.2016.108.

[2] A. Kolhatkar, A. Jamison, D. Litvinov, R. Willson, and T. Lee, 'Tuning the Magnetic Properties of Nanoparticles', *Int. J. Mol. Sci.*, vol. 14, no. 8, pp. 15977–16009, Jul. 2013, doi: 10.3390/ijms140815977.

[3] K. A. Majorek *et al.*, 'Structural and immunologic characterization of bovine, horse, and rabbit serum albumins', *Mol. Immunol.*, vol. 52, no. 3–4, pp. 174–182, Oct. 2012, doi: 10.1016/j.molimm.2012.05.011.

[4] A. Herraiz *et al.*, 'A single-step radiolabeling strategy for PET, SPECT, and therapeutic radionuclides using nanoparticles as a universal chelator', *Npj Imaging*, vol. 4, no. 1, p. 8, Feb. 2026, doi: 10.1038/s44303-026-00142-1.

[5] A. Herraiz *et al.*, 'Periodic table screening for enhanced positive contrast in MRI and *in vivo* uptake in glioblastoma', *Chem. Sci.*, vol. 15, no. 22, pp. 8578–8590, 2024, doi: 10.1039/D4SC01069H.

[6] T. Lammers, S. Aime, W. E. Hennink, G. Storm, and F. Kiessling, 'Theranostic Nanomedicine', *Acc. Chem. Res.*, vol. 44, no. 10, pp. 1029–1038, Oct. 2011, doi: 10.1021/ar200019c.

[7] I. Fernández-Barahona, M. Muñoz-Hernando, J. Pellico, J. Ruiz-Cabello, and F. Herranz, 'Molecular Imaging with 68Ga Radio-Nanomaterials: Shedding Light on Nanoparticles', *Appl. Sci.*, vol. 8, no. 7, p. 1098, Jul. 2018, doi: 10.3390/app8071098.

[8] H. Maeda, J. Wu, T. Sawa, Y. Matsumura, and K. Hori, 'Tumor vascular permeability and the EPR effect in macromolecular therapeutics: a review', *J. Controlled Release*, vol. 65, no. 1–2, pp. 271–284, Mar. 2000, doi: 10.1016/S0168-3659(99)00248-5.

[9] E. Blanco, H. Shen, and M. Ferrari, 'Principles of nanoparticle design for overcoming biological barriers to drug delivery', *Nat. Biotechnol.*, vol. 33, no. 9, pp. 941–951, Sep. 2015, doi: 10.1038/nbt.3330.

[10] J. Xie, S. Lee, and X. Chen, 'Nanoparticle-based theranostic agents', *Adv. Drug Deliv. Rev.*, vol. 62, no. 11, pp. 1064–1079, Aug. 2010, doi: 10.1016/j.addr.2010.07.009.

[11] S. S. Kelkar and T. M. Reineke, 'Theranostics: Combining Imaging and Therapy', *Bioconjug. Chem.*, vol. 22, no. 10, pp. 1879–1903, Oct. 2011, doi: 10.1021/bc200151q.

[12] M. S. Muthu, D. T. Leong, L. Mei, and S.-S. Feng, 'Nanotheranostics - Application and Further Development of Nanomedicine Strategies for Advanced Theranostics', *Theranostics*, vol. 4, no. 6, pp. 660–677, 2014, doi: 10.7150/thno.8698.

[13] Dan Peer1†, Jeffrey M. Karp2,3†, Seungpyo Hong4†, Omid C. Farokhzad5, , and Rimona Margalit6, 'Nanocarriers as an emerging platform for cancer therapy'. Nature Publishing Group, 2007. [Online]. Available: www.nature.com/naturenanotechnology

[14] D. Rosenblum, N. Joshi, W. Tao, J. M. Karp, and D. Peer, 'Progress and challenges towards targeted delivery of cancer therapeutics', *Nat. Commun.*, vol. 9, no. 1, p. 1410, Apr. 2018, doi: 10.1038/s41467-018-03705-y.

[15] Q. A. Pankhurst, J. Connolly, S. K. Jones, and J. Dobson, 'Applications of magnetic nanoparticles in biomedicine'.

[16] S. M. Janib, A. S. Moses, and J. A. MacKay, 'Imaging and drug delivery using theranostic nanoparticles', *Adv. Drug Deliv. Rev.*, vol. 62, no. 11, pp. 1052–1063, Aug. 2010, doi: 10.1016/j.addr.2010.08.004.

[17] J. Pellico, 'Nano-radiotrazadores y Nanopartículas superparamagnéticas: Síntesis, propiedades y aplicación en imagen molecular', Universidad Complutense de Madrid, 2016.

[18] I. Barahona, 'Nanomaterials for multimodal molecular imaging', Universidad Complutense de Madrid, 2022.

[19] S. Laurent *et al.*, 'Magnetic Iron Oxide Nanoparticles: Synthesis, Stabilization, Vectorization, Physicochemical Characterizations, and Biological Applications', *Chem. Rev.*, vol. 108, no. 6, pp. 2064–2110, Jun. 2008, doi: 10.1021/cr068445e.

[20] D. Bobo, K. J. Robinson, J. Islam, K. J. Thurecht, and S. R. Corrie, 'Nanoparticle-Based Medicines: A Review of FDA-Approved Materials and Clinical Trials to Date', *Pharm. Res.*, vol. 33, no. 10, pp. 2373–2387, Oct. 2016, doi: 10.1007/s11095-016-1958-5.

[21] H. Arami, A. Khandhar, D. Liggitt, and K. M. Krishnan, 'In vivo delivery, pharmacokinetics, biodistribution and toxicity of iron oxide nanoparticles', *Chem. Soc. Rev.*, vol. 44, no. 23, pp. 8576–8607, 2015, doi: 10.1039/C5CS00541H.

[22] M. U. Muckenthaler, S. Rivella, M. W. Hentze, and B. Galy, 'A Red Carpet for Iron Metabolism', *Cell*, vol. 168, no. 3, pp. 344–361, Jan. 2017, doi: 10.1016/j.cell.2016.12.034.

[23] A. D. Nehe and A. D. Kulkarni, 'Fundamentals of Superparamagnetic Iron Oxide Nanoparticles: Recent Update', *J. Microsc. Ultrastruct.*, vol. 13, no. 3, pp. 113–129, Jul. 2025, doi: 10.4103/jmau.jmau_17_22.

[24] S. Xu, G. Zhang, J. Zhang, W. Liu, Y. Wang, and X. Fu, 'Advances in Brain Tumor Therapy Based on the Magnetic Nanoparticles', *Int. J. Nanomedicine*, vol. Volume 18, pp. 7803–7823, Dec. 2023, doi: 10.2147/IJN.S444319.

[25] C. F. G. C. Geraldes and S. Laurent, 'Classification and basic properties of contrast agents for magnetic resonance imaging', *Contrast Media Mol. Imaging*, vol. 4, no. 1, pp. 1–23, Jan. 2009, doi: 10.1002/cmmi.265.

[26] H. B. Na, I. C. Song, and T. Hyeon, 'Inorganic Nanoparticles for MRI Contrast Agents', *Adv. Mater.*, vol. 21, no. 21, pp. 2133–2148, Jun. 2009, doi: 10.1002/adma.200802366.

[27] E. J. Werner, A. Datta, C. J. Jocher, and K. N. Raymond, 'High-Relaxivity MRI Contrast Agents: Where Coordination Chemistry Meets Medical Imaging', *Angew. Chem. Int. Ed.*, vol. 47, no. 45, pp. 8568–8580, Oct. 2008, doi: 10.1002/anie.200800212.

[28] N. Lee, D. Yoo, D. Ling, M. H. Cho, T. Hyeon, and J. Cheon, 'Iron Oxide Based Nanoparticles for Multimodal Imaging and Magnetoresponsive Therapy', *Chem. Rev.*, vol. 115, no. 19, pp. 10637–10689, Oct. 2015, doi: 10.1021/acs.chemrev.5b00112.

[29] A. E. Nel *et al.*, 'Understanding biophysicochemical interactions at the nano–bio interface', *Nat. Mater.*, vol. 8, no. 7, pp. 543–557, Jul. 2009, doi: 10.1038/nmat2442.

[30] S. Laurent *et al.*, 'Magnetic Iron Oxide Nanoparticles: Synthesis, Stabilization, Vectorization, Physicochemical Characterizations, and Biological Applications', *Chem. Rev.*, vol. 108, no. 6, pp. 2064–2110, Jun. 2008, doi: 10.1021/cr068445e.

[31] S. Laurent *et al.*, 'Magnetic Iron Oxide Nanoparticles: Synthesis, Stabilization, Vectorization, Physicochemical Characterizations, and Biological Applications', *Chem. Rev.*, vol. 108, no. 6, pp. 2064–2110, Jun. 2008, doi: 10.1021/cr068445e.

[32] D. Owensiii and N. Peppas, 'Opsonization, biodistribution, and pharmacokinetics of polymeric nanoparticles', *Int. J. Pharm.*, vol. 307, no. 1, pp. 93–102, Jan. 2006, doi: 10.1016/j.ijpharm.2005.10.010.

[33] F. Kratz, 'Albumin as a drug carrier: Design of prodrugs, drug conjugates and nanoparticles', *J. Controlled Release*, vol. 132, no. 3, pp. 171–183, Dec. 2008, doi: 10.1016/j.jconrel.2008.05.010.

[34] M. M. Bradford, "A rapid and sensitive method for the quantitation of microgram quantities of protein utilizing the principle of protein-dye binding," Anal. Biochem., vol. 72, no. 1–2, pp. 248–254, May 1976, doi: 10.1016/0003-2697(76)90527-3.

[35] J. V. Gregory et al., "Systemic brain tumor delivery of synthetic protein nanoparticles for glioblastoma therapy," Nat. Commun., vol. 11, no. 1, p. 5687, Nov. 2020, doi: 10.1038/s41467-020-19225-7.

[36] H. Mohammad, M. Darwish, G. Katona, and I. Csóka, "Functionalized albumin nanoparticles: A multifunctional platform for enhanced brain drug delivery," Mater. Today Bio, vol. 35, p. 102616, 2025, doi: 10.1016/j.mtbio.2025.102616.

[37] C.-E. Tincu, C. V. Andrițoiu, M. Popa, and L. Ochiuz, "Recent advancements and strategies for overcoming the blood-brain barrier using albumin-based drug delivery systems to treat brain cancer, with a focus on glioblastoma," Polymers, vol. 15, no. 19, p. 3969, Oct. 2023, doi: 10.3390/polym15193969.

[38] Thermo Fisher Scientific, "Carbodiimide Crosslinker Chemistry - US." Thermo Fisher Scientific. [Online]. Available: https://www.thermofisher.com/us/en/home/life-science/protein-biology. [Accessed: Feb. 23, 2025].

[39] Y. Miao, "Application of BSA-bioconjugated phosphorescence nanohybrids in protein detection in biofluids," RSC Adv., vol. 5, no. 94, pp. 76804-76812, Aug. 2015, doi: 10.1039/C5RA11691K.

[40] Pellico, J. et al. (2017). One-Step Fast Synthesis of Nanoparticles for MRI: Coating Chemistry as the Key Variable Determining Positive or Negative Contrast. Langmuir, 33(39), 10239-10247. https://doi.org/10.1021/acs.langmuir.7b01759

[41] Dumitrache, F. et al. (2025). Experimental Study Regarding the Synthesis of Iron Oxide Nanoparticles by Laser Pyrolysis Using Ethanol as Sensitizer; Morpho-Structural Alterations Using Thermal Treatments on the Synthesized Nanoparticles. Coatings, 15(2), 234. https://doi.org/10.3390/coatings15020234

[42] Rasmussen, M. K. et al. (2020). Size and surface charge characterization of nanoparticles with a salt gradient. Nature Communications. https://doi.org/10.1038/s41467-020-15889-3

[43] B. C. Smith, Fundamentals of Fourier Transform Infrared Spectroscopy. Boca Raton, FL, USA: CRC Press, 2011.

[44] A. Giustiniani, "Linking adhesive properties and pore organisation of silicone emulsions obtained by reactive blending," Ph.D. dissertation, Université Paris-Saclay, Paris, France, 2017.

[45] I. Solomon, "Relaxation processes in a system of two spins," Phys. Rev., vol. 99, no. 2, pp. 559–565, Jul. 1955.

[46] N. Bloembergen and L. O. Morgan, "Proton relaxation times in paramagnetic solutions," J. Chem. Phys., vol. 34, no. 3, pp. 842–850, Mar. 1961.

[47] S. Laurent et al., "Magnetic iron oxide nanoparticles: Synthesis, stabilization, vectorization, physicochemical characterizations, and biological applications," Chem. Rev., vol. 108, no. 6, pp. 2064–2110, Jun. 2008, doi: 10.1021/cr068445e.